Petrologie sedimentárních hornin

LS, 1.roč.

5. Kaustobiolity, silicity, ferolity, fosfáty, evapority

Karel Martínek

Ústav geologie a paleontologie

Organická hmota, kaustobiolity

uhlí - huminové, sapropelové, prouhelnění, antracit; uh. petrologie, macerály (vitrinit, inertinit, exinit)

černé břidlice - bitumen, typy kerogenu, pyrolýza, Van Krevelenův diagram

ropa - ropné okno, generování tekutých uhlovodíků -> tlak fluid, hydraulické fraktury

degradace, maturace org. hmoty; alterace, diageneze, katageneze termální zralost OM, odraznost vitrinitu

uhlí

Table 4.4 **Summary of changes in some bulk characteristics of coal with increasing rank** (After Teichmüller and Teichmüller, 1968)

	Rank stages		ASTM classification*	%C†	% volatiles†	% water	%R‡	Calorific value (kcal/kg)§
				60		75	0.25	
BROWN COAL	SOFT BROWN COAL		Brown coal		53	35	0.3	4000
BROWN COAL	HARD BROWN COAL	Dull	Lignite	71	49	25		5500
BROWN COAL	HARD BROWN COAL	Bright	Sub-bituminous coal	77	42	10	0.5	7000
HARD COAL	BITUMINOUS HARD COAL	Low rank	High volatile / Medium volatile / Low volatile (Bituminous coal)	87	29		1.1	8650
HARD COAL	BITUMINOUS HARD COAL	High rank	Semi-anthracite	91	8		2.5	8650
HARD COAL	ANTHRACITE		Anthracite / Meta-anthracite	100	0	0	11.0	

* American Society for Testing and Materials.
† As % of dry ash-free weight.
‡ Vitrinite reflectance (see Section 5.6.2).
§ Ash-free value.

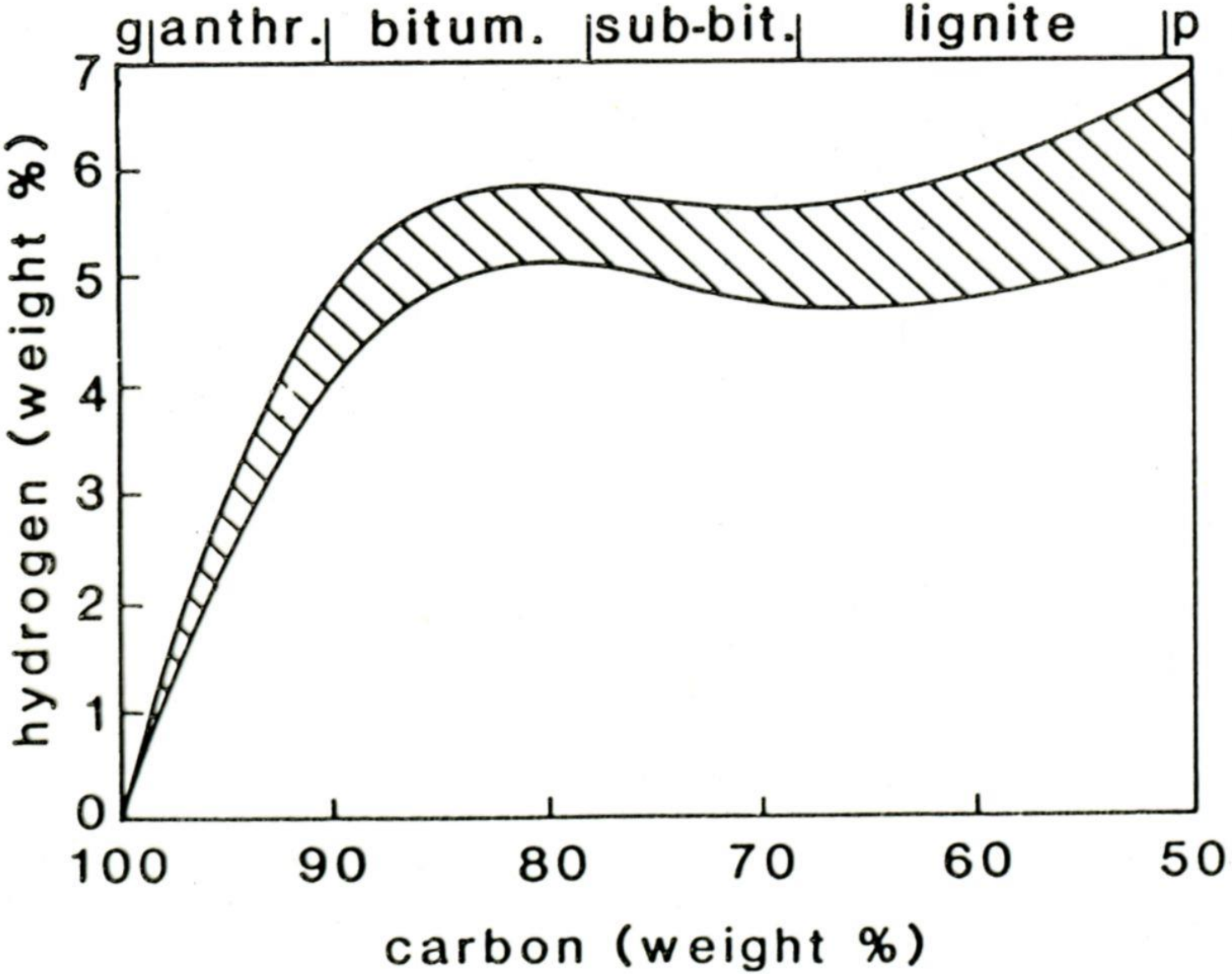
g
anthr.
bitum.
sub-bit.
lignite
p
hydrogen (weight %)
0
1
2
3
4
5
6
7
100
90
80
70
60
50
carbon (weight %)

Table 4.3 **Coal maceral groups**

Maceral groups	*Macerals*	*General properties*
Vitrinite	Telinite Collinite	Angular to subangular particles, sometimes show cell structure. Moderate transmittance. Fluorescence usually absent. Intermediate reflectance.
Inertinite	Micrinite Sclerotinite Semi-fusinite Fusinite	Angular, often cellular outline or granular texture. Opaque in transmitted light. No fluorescence. High reflectance.
Exinite	Alginite Sporinite Cutinite Suberinite Resinite Cerinite	Characteristic shape, e.g. algae, resins, spores. High transmittance. Intense fluorescence (at low maturity). Relatively low reflectance.

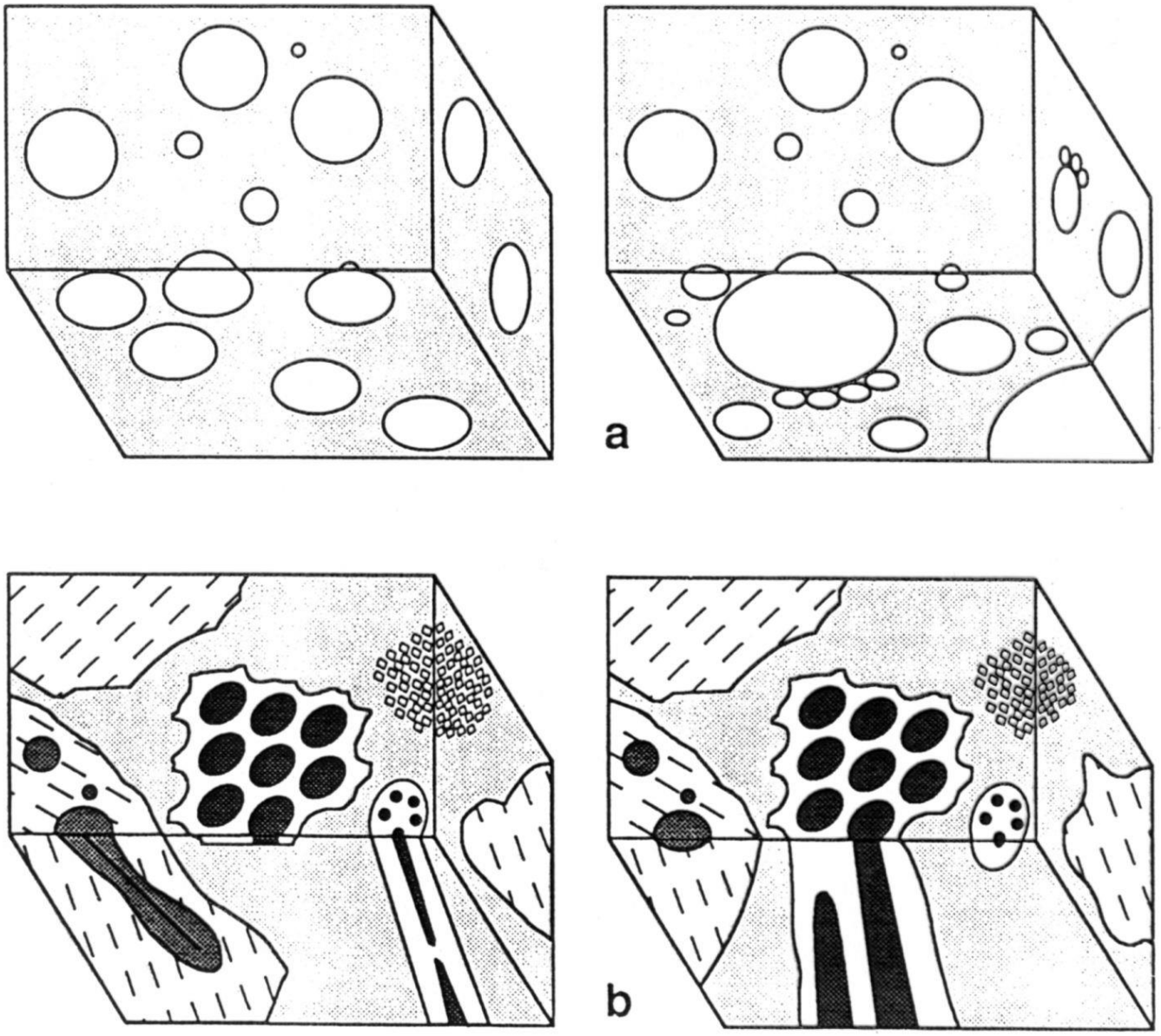

Fig. 7.33. The stereological problem: a) circles of varying diameters on the observed section (top surface) may arise from spheres of one size or a variety of sizes; b) the exact size and morphology of an individual particle in three dimensions cannot be determined from observation of a two- dimensional cross section.

původ organické hmoty - van Krevelenův diagram

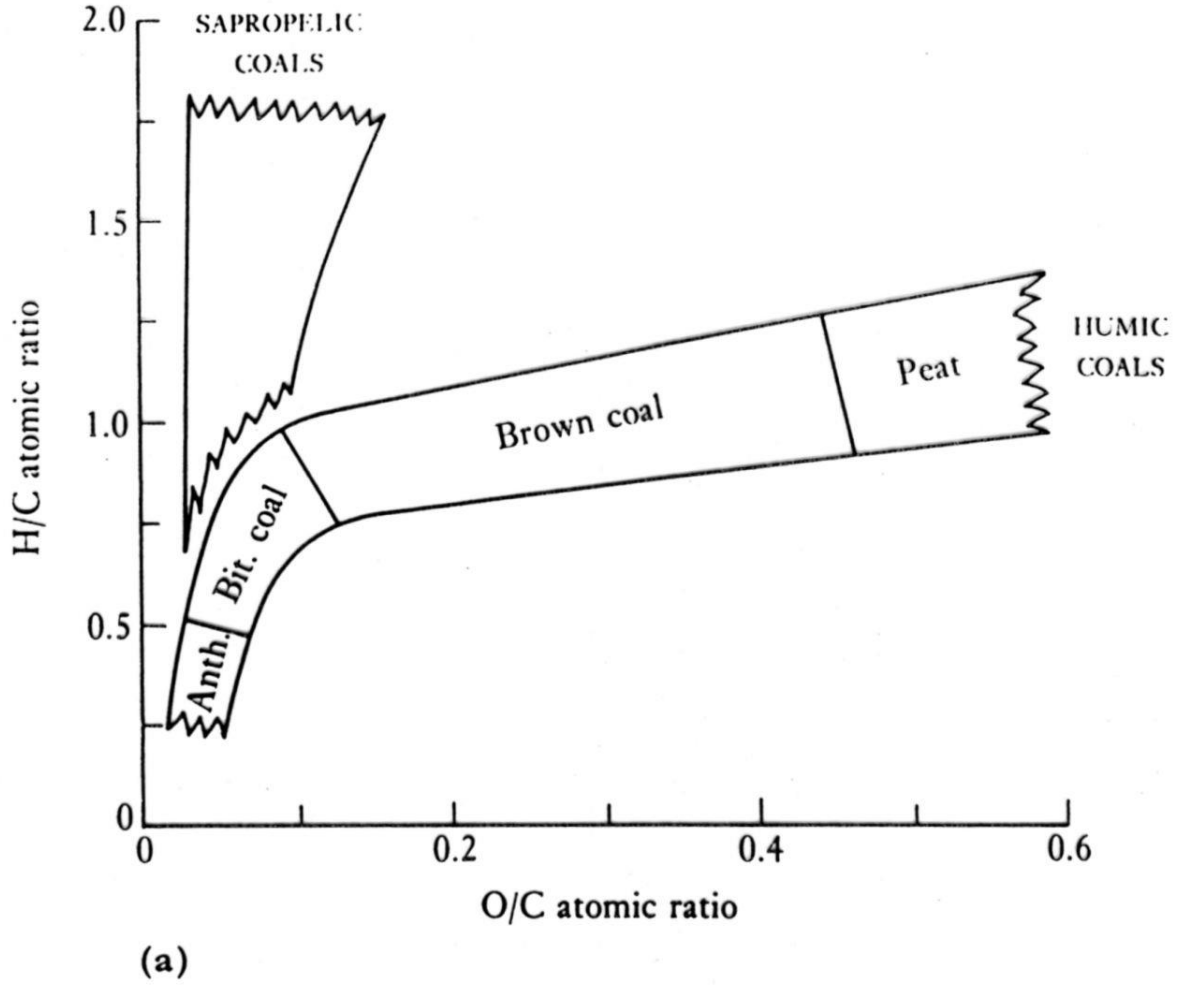

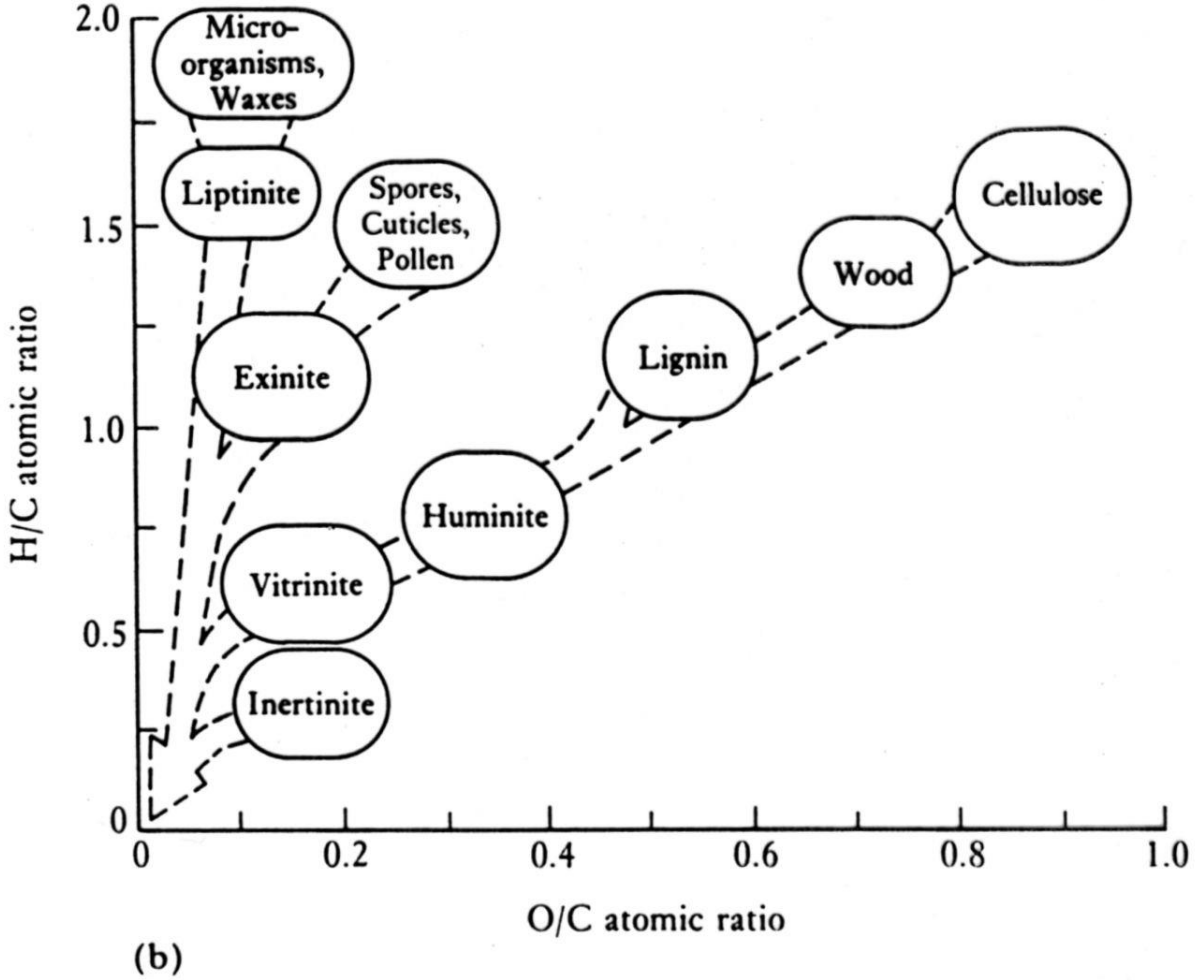

Figure 4.2 (a) Van Krevelen diagram showing the main evolutionary trends of sapropelic (cannel and boghead) and humic coals. Four stages are denoted for humic coals, in order of increasing rank: peat, brown coal, bituminous hard coal and anthracite. (b) Van Krevelen diagram showing the position of the main coal macerals and their diagenetic, evolutionary relationships to various components in living organisms (see Section 4.4.2 for an explanation of liptinite).

černé břidlice

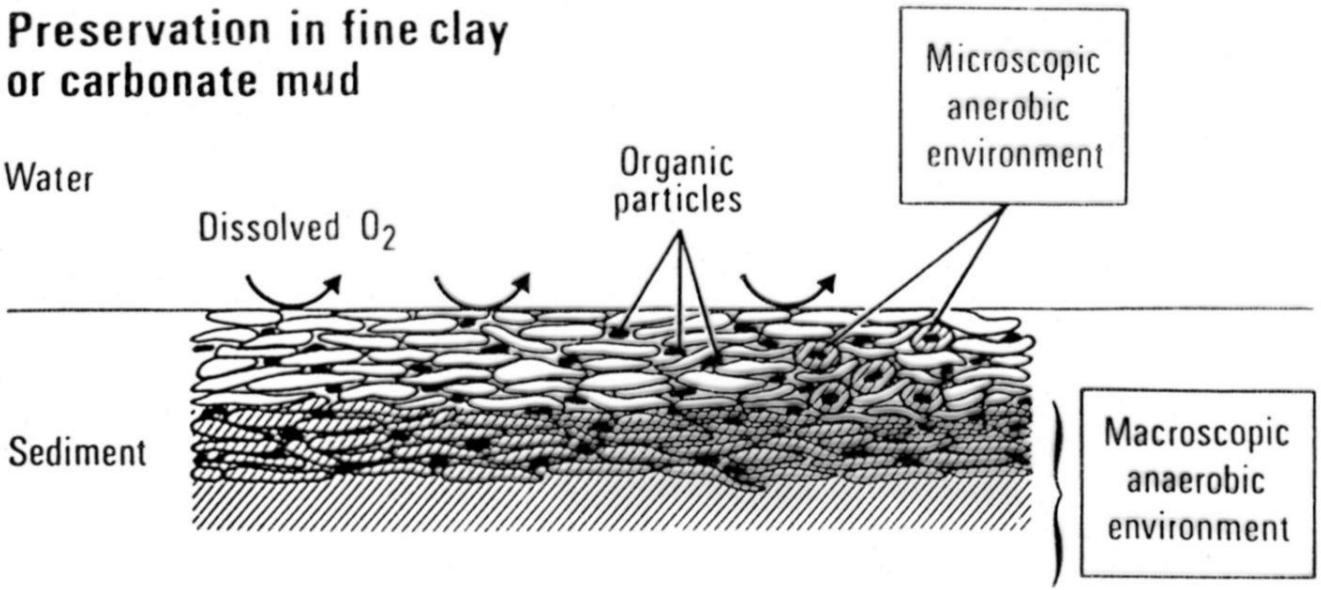

Destruction in a porous sediment deposited under aerobic conditions

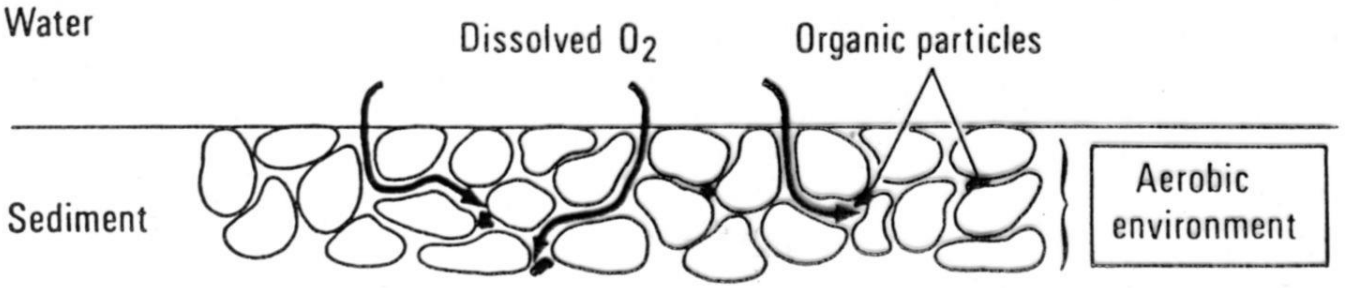

Fig. II.2.1. Preservation or destruction of the organic matter in a freshly deposited sediment. In a fine clay or carbonate mud *(top)*, pore water becomes a nearly closed microenvironment. There is no replenishment of oxygen, and anaerobic conditions are rapidly established, first on microscopic, then on a macroscopic scale. In a porous sand deposited under aerobic conditions *(bottom)*, free circulation of water containing dissolved oxygen results in the destruction of the organic matter

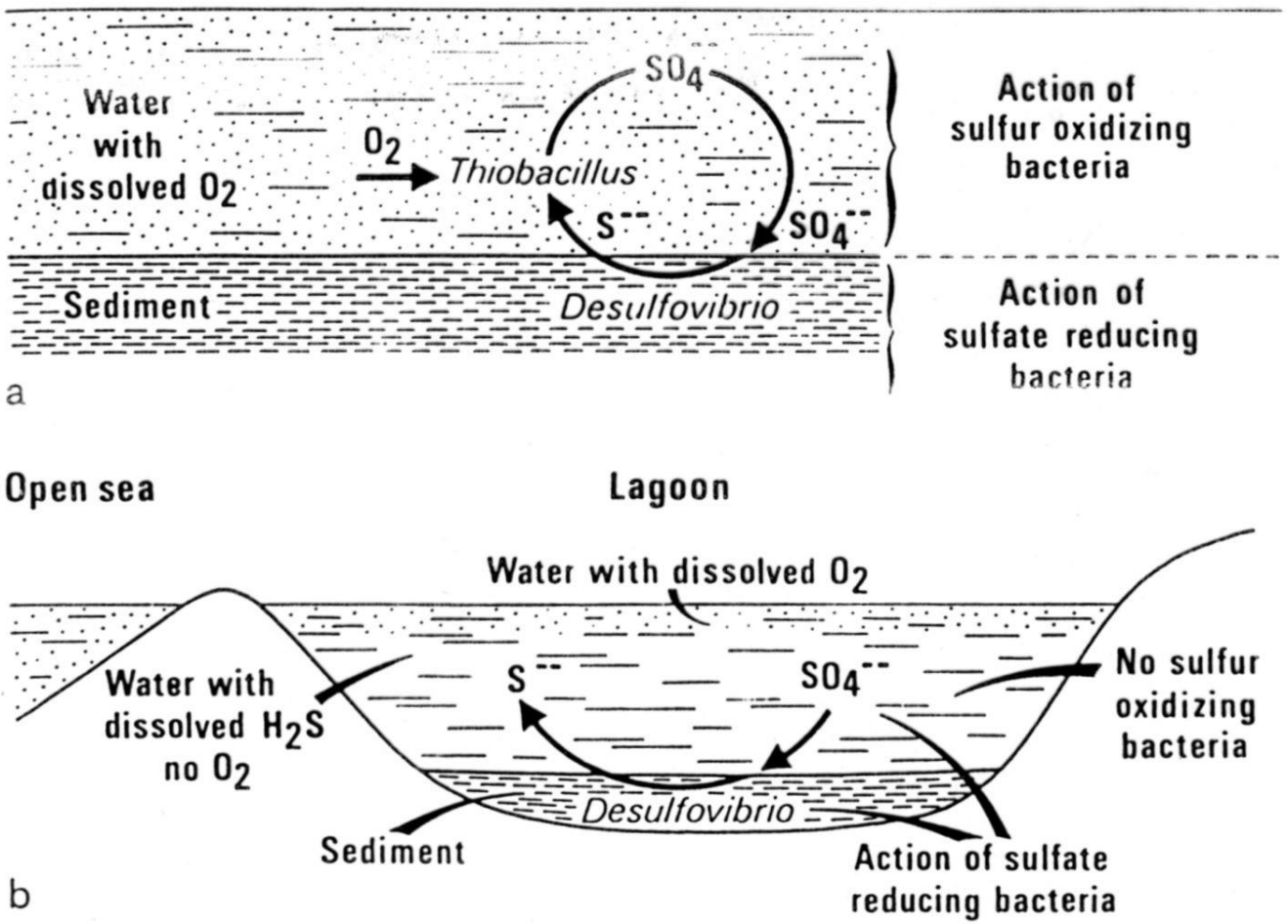

Fig. II.2.2 a and b. Formation and destruction of hydrogen sulfide in sediments and bottom waters. (a) Open sea conditions: there is an equilibrium between formation and destruction of hydrogen sulfide. (b) Restricted water circulation: no dissolved oxygen in bottom waters. This results in the absence of aerobic sulfur-oxidizing bacteria. Thus, there is no destruction of hydrogen sulfide in bottom waters, which are anoxic and contain H_2S

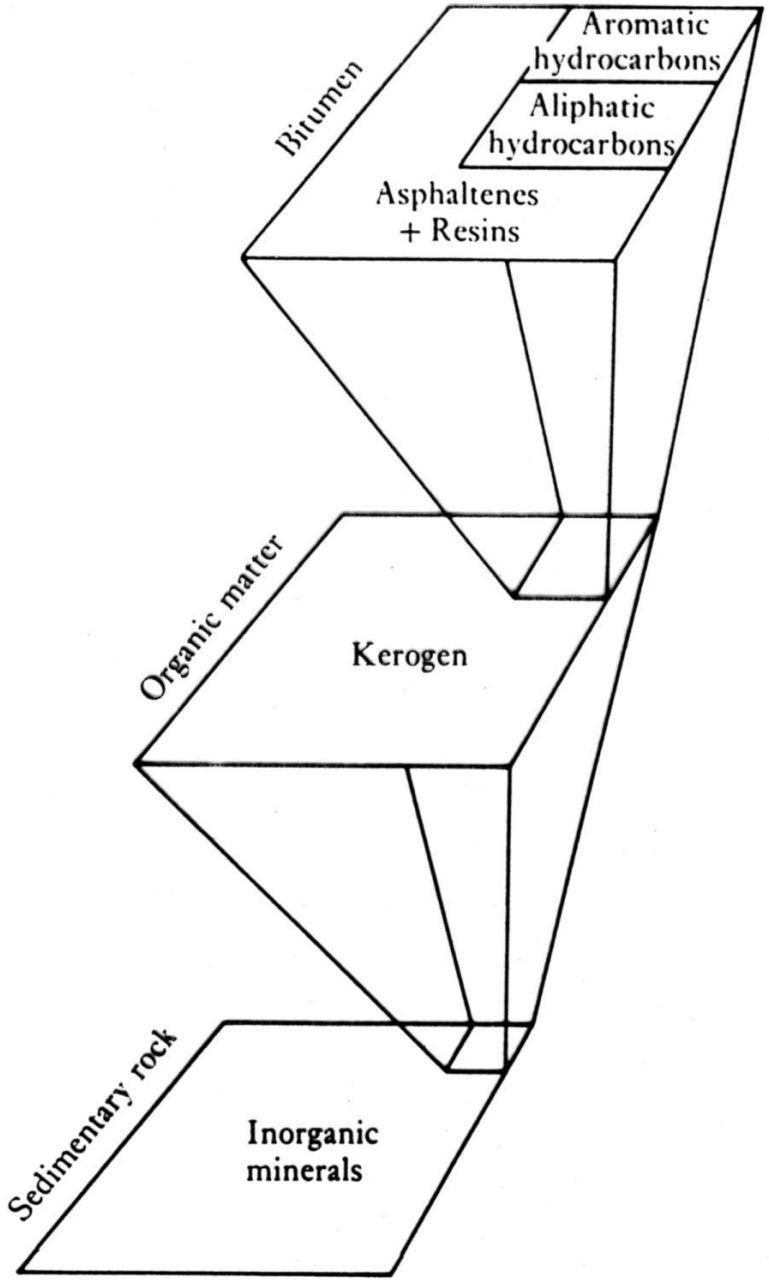

Figure 4.5 Composition of disseminated organic matter in sedimentary rocks. (After Tissot and Welte, 1984.)

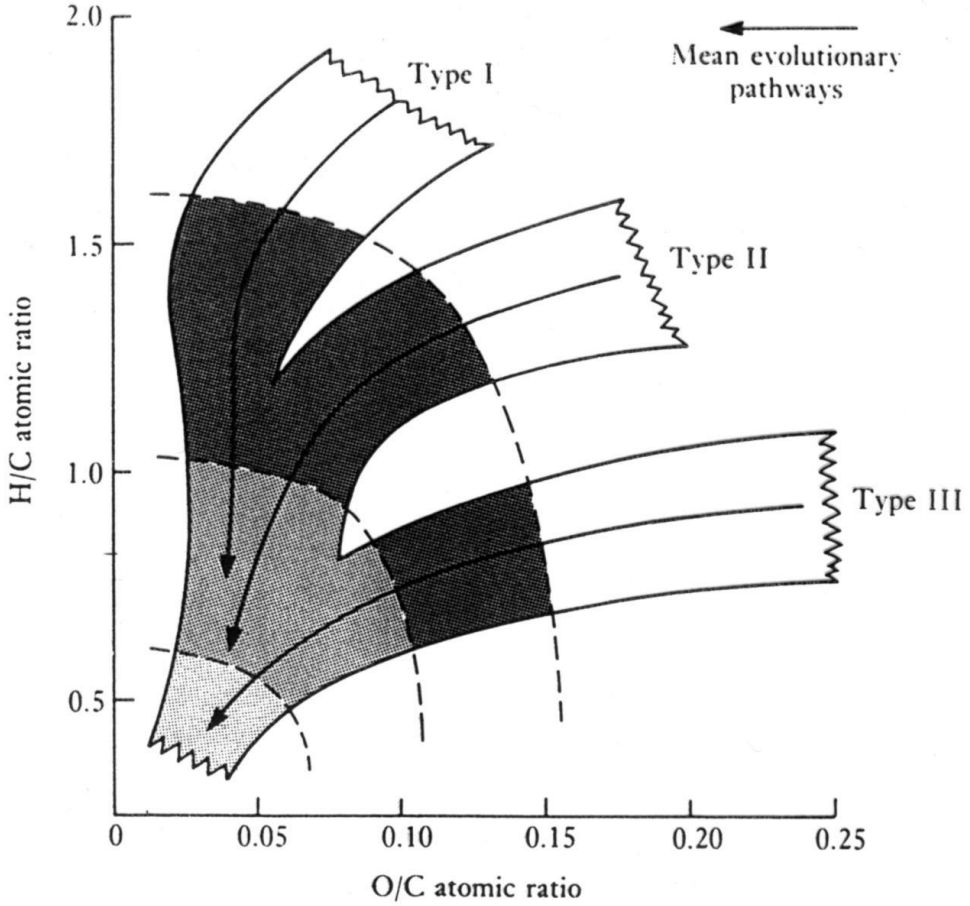

Fluids evolved	*Zone*	*Stage*
Carbon dioxide and water	Immature	Diagenesis
Liquid hydrocarbons	Oil	Catagenesis
Gaseous hydrocarbons (C_1–C_4)	Wet gas (condensate)	
Methane	Dry gas	Metagenesis

Figure 4.10 Van Krevelen diagram showing the evolution paths of the three hydrocarbon-generating types of kerogen and the main fluids evolved at different stages of maturity (N.B. not all type III kerogens generate oil). (After Durand, 1980.)

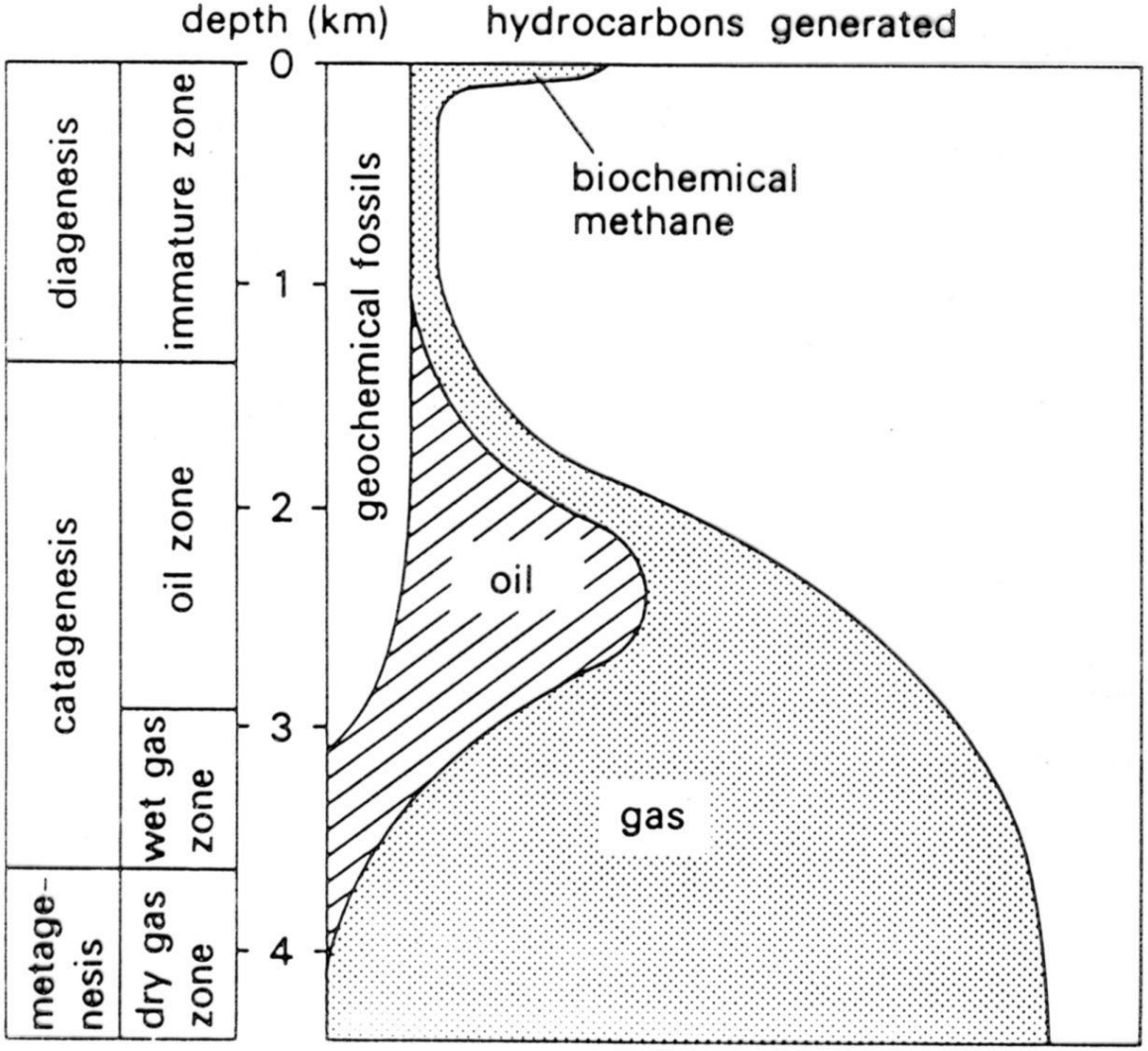

Fig. 8.8 Hydrocarbon generation with depth from organic matter, mainly kerogen contained in sediments. The precise depth at which hydrocarbons are evolved depends on the geothermal gradient, the burial history, and type of kerogen present. After Tissot & Welte (1984).

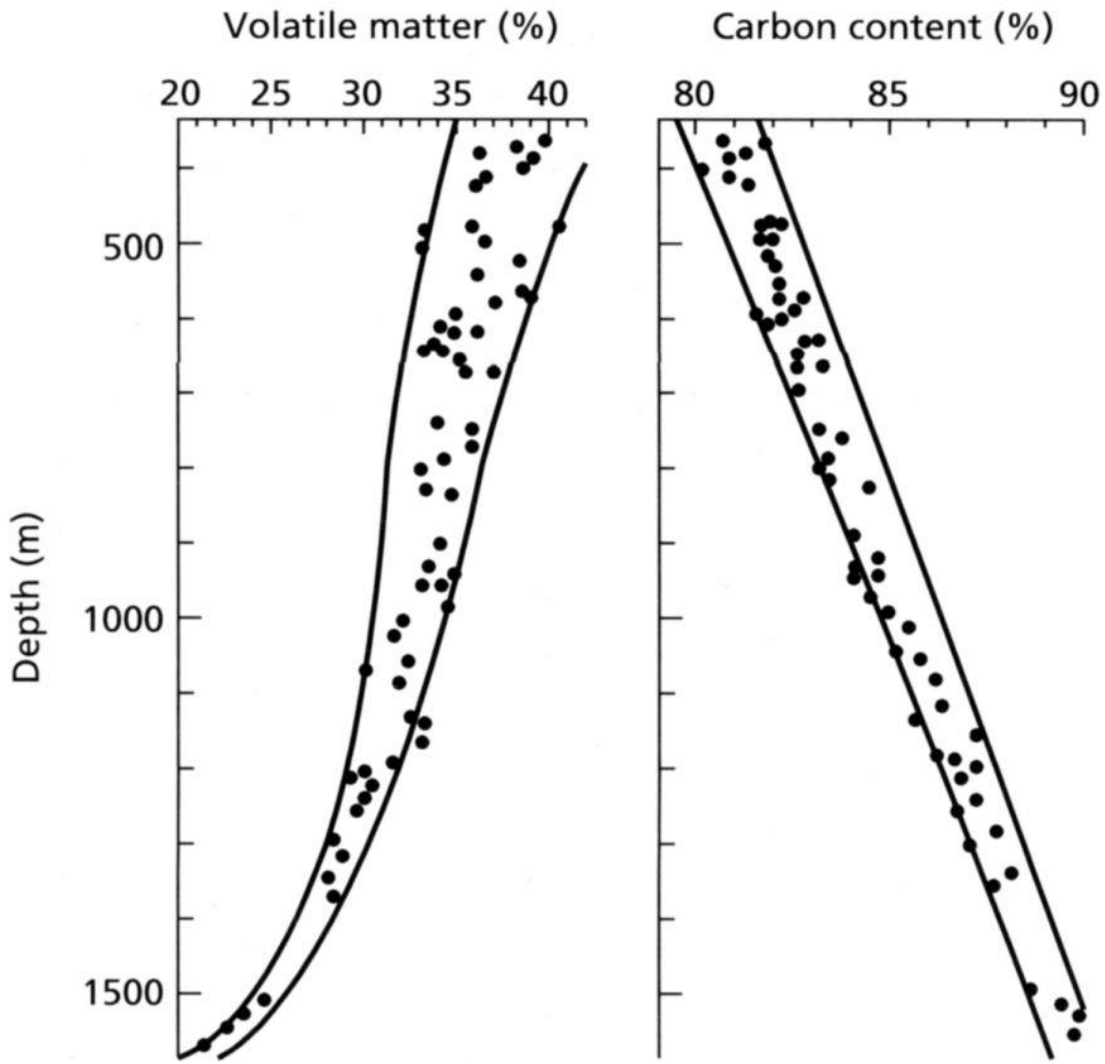

Fig. 8.4 An example from the Carboniferous Westphalian Coal Measures of Germany of the increase in coal rank with depth, on the basis of volatile matter and carbon contents (both dry-ash free). After Teichmuller (1987).

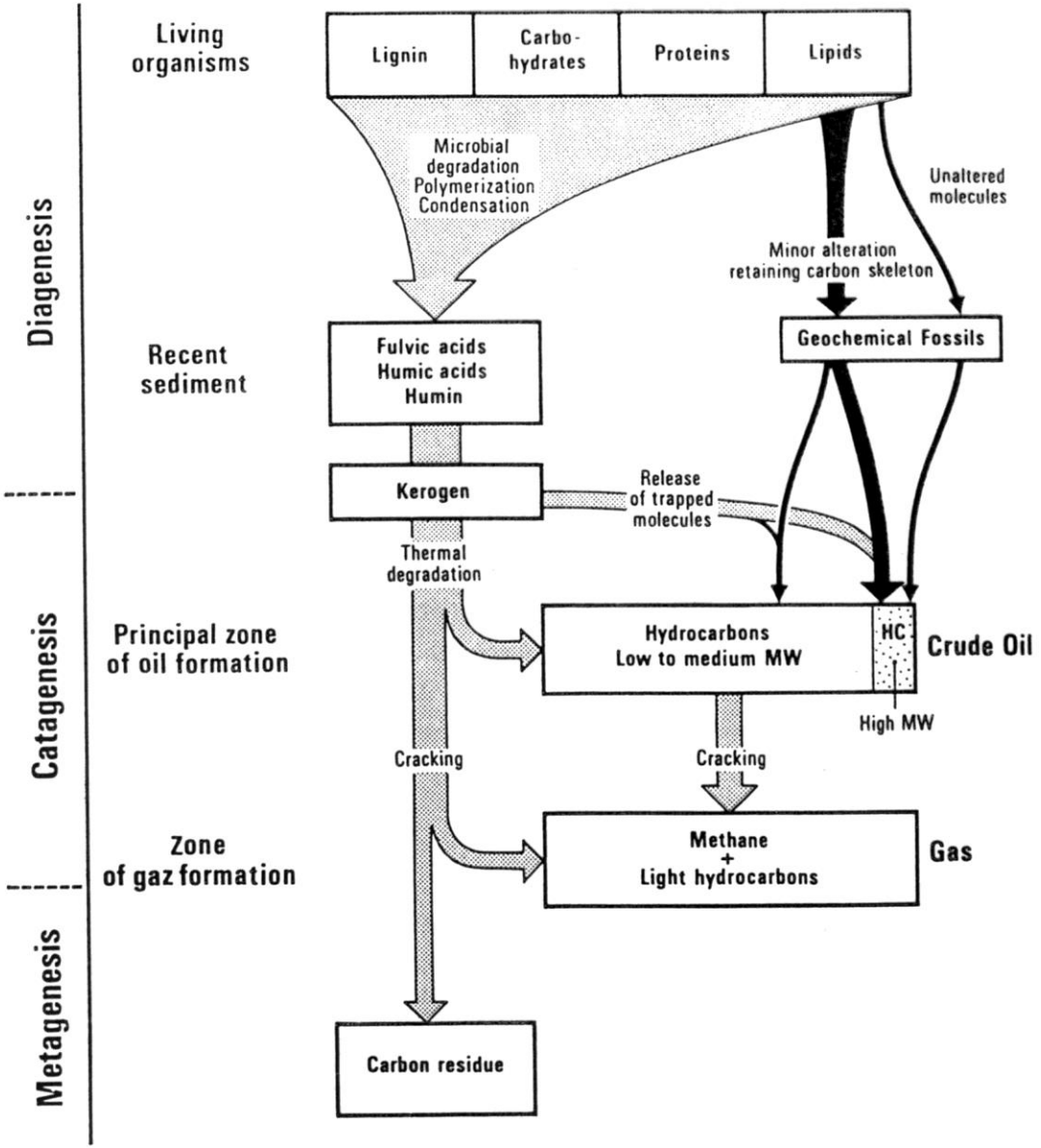

Fig. II.3.1. Sources of hydrocarbons in geological situations, with regard to the evolution of organic matter. Geochemical fossils represent a first source of hydrocarbons in the subsurface *(black solid arrows)*. Degradation of kerogen represents a second source of hydrocarbons *(grey dotted arrows)*

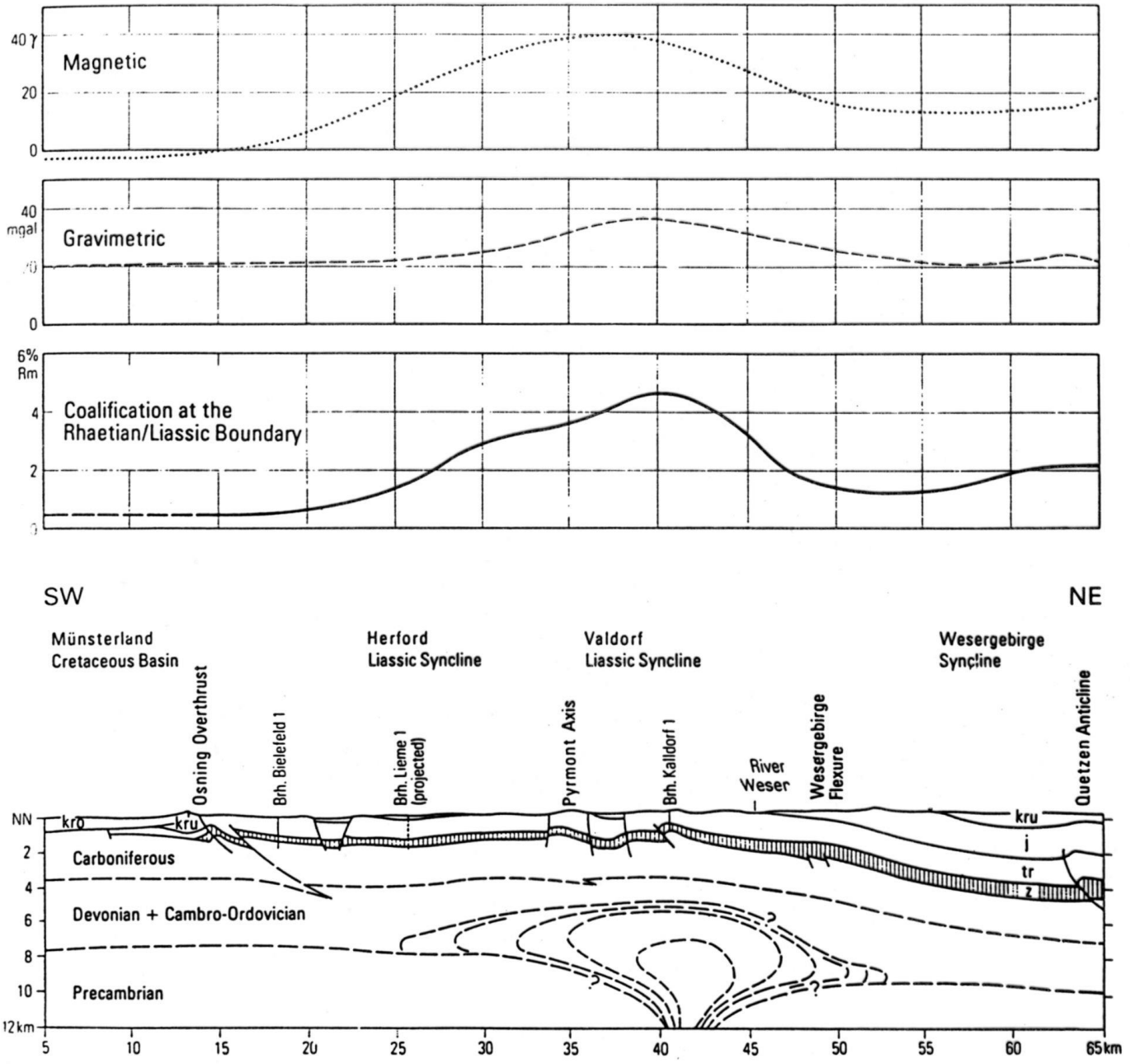

Fig. 8.27. Section across the Vlotho Massif on the basis of magnetics, gravimetry and vitrinite reflectance. (After Deutloff et al., 1980).

Silicity

z hlediska petrologie nevhodná synonyma: lydit (proterozoický silicit), buližník (ordovický silicit), limnokvarcit (silicit jezerního původu), sluňák (valoun silkrety)

mineralogie - opál A, opál CT, křemen

mikrostruktury - euhedrální, mikrokřemen, megakřemen, chalcedonický kř.
zdroje, rozpustnost

diageneze, silicifikace mořská vs. jezerní (slaná alkalická jezera)

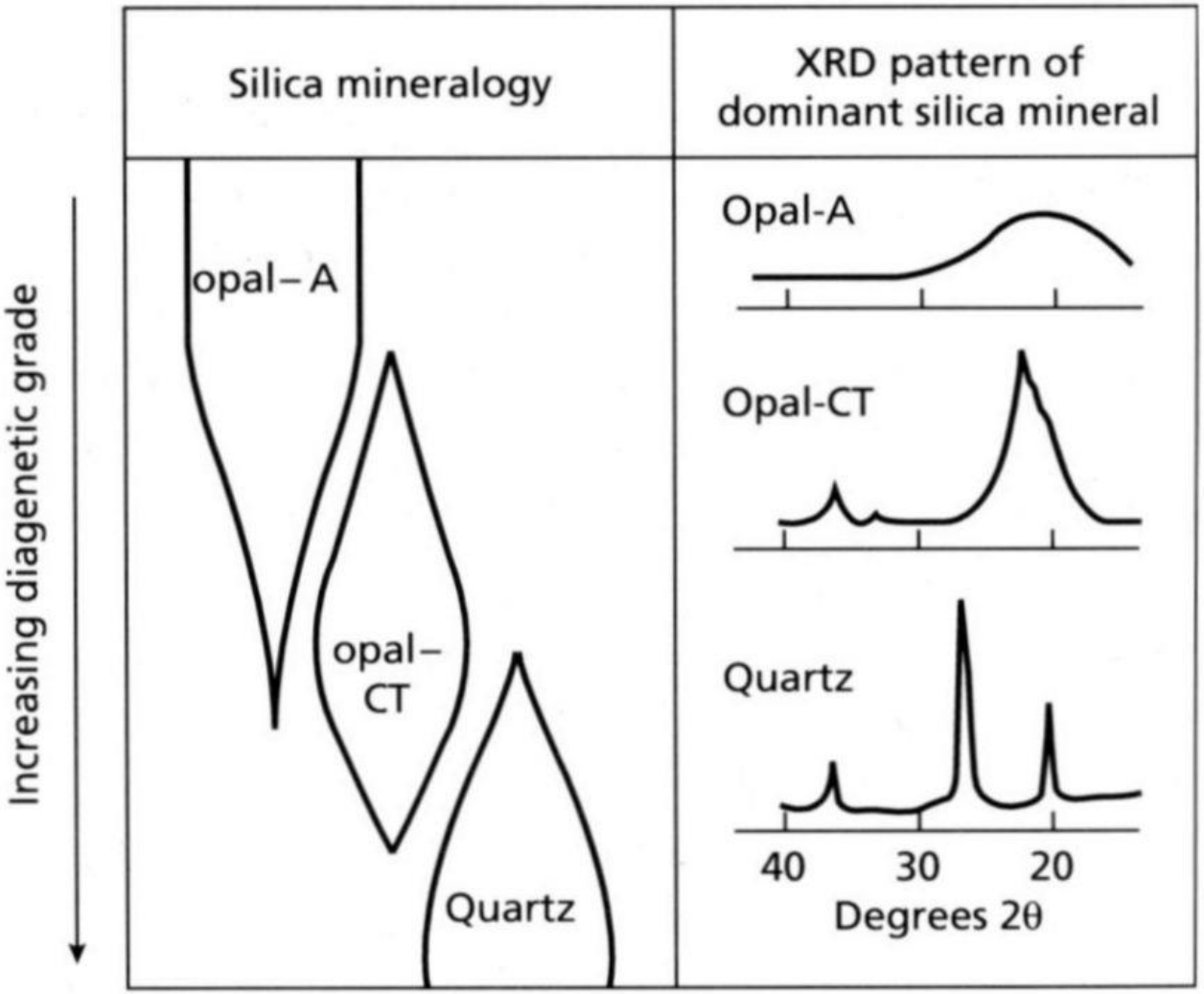

Fig. 9.6 Schematic changes in silica mineralogy with increasing diagenesis, and X-ray diffraction patterns for opal-A, opal-CT and quartz showing the increasing crystallinity. After Pisciotto (1981).

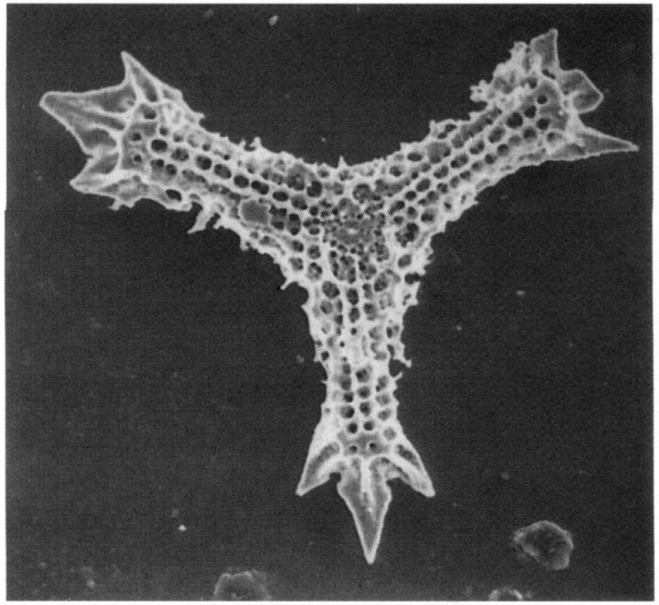

(a)

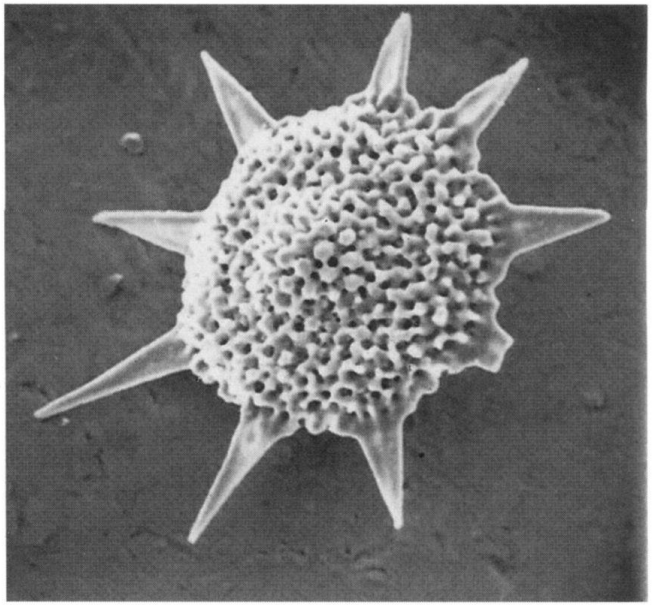

(

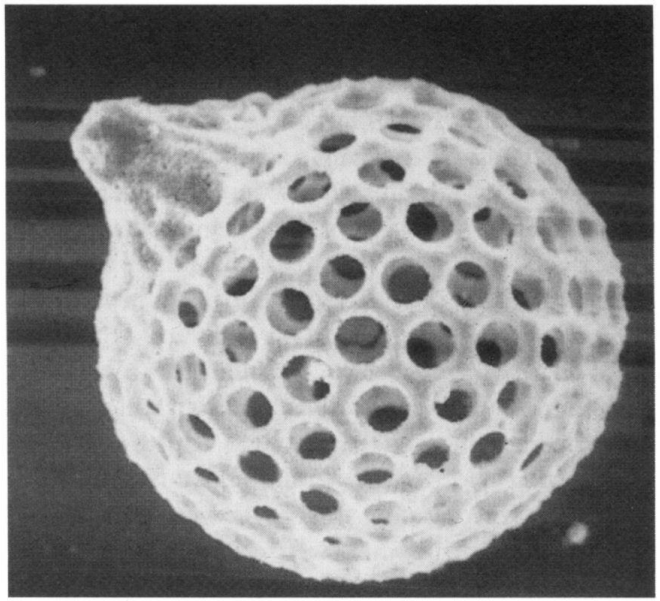

(c)

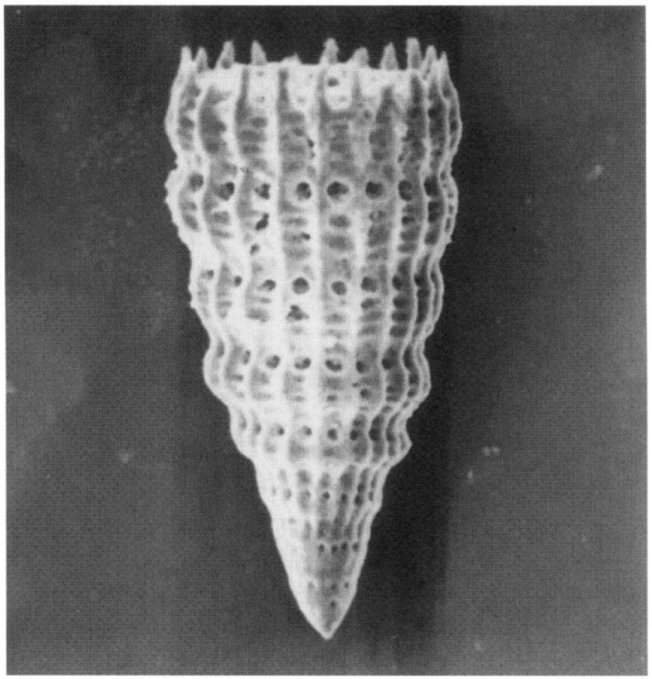

(

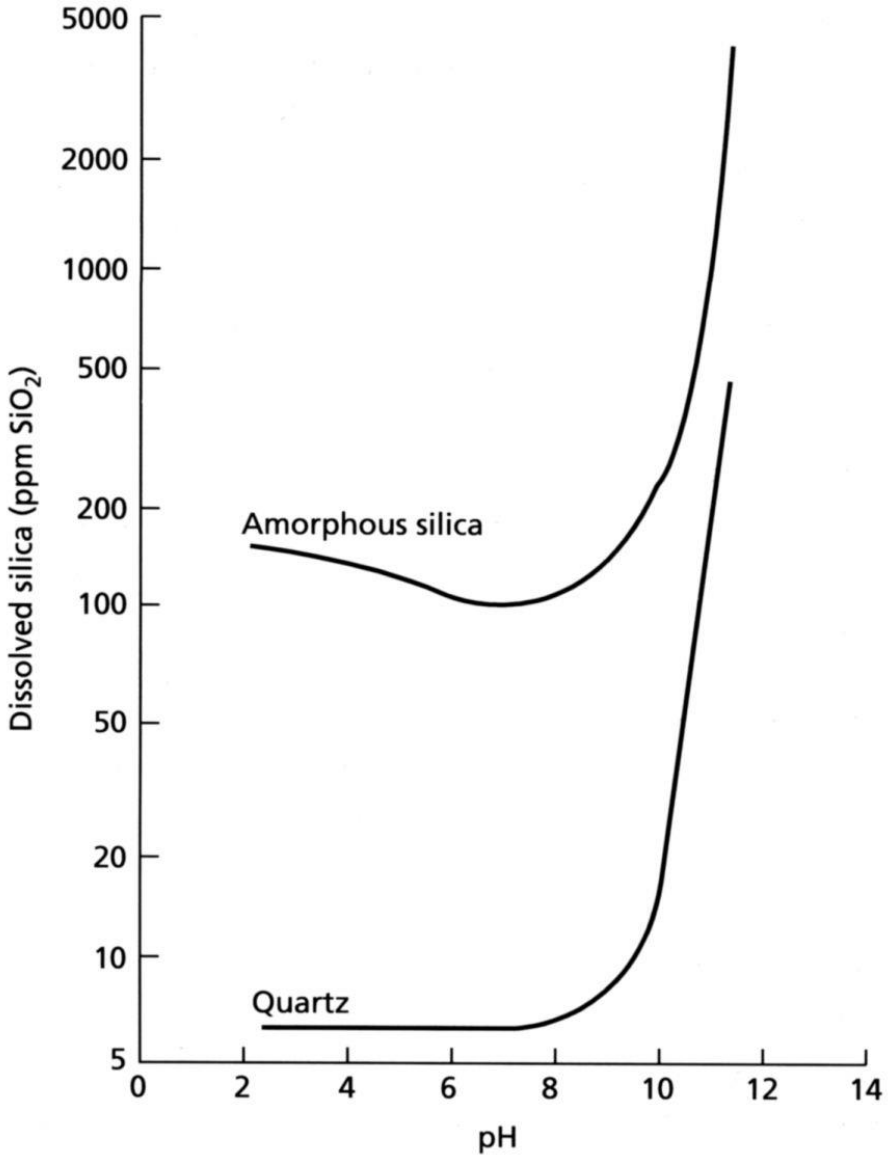

Fig. 9.8 The solubility of quartz and amorphous silica at 25 °C. At pH values less than 9, the silica is in solution as undissolved orthosilicic acid (H_4SiO_4); above pH 9, this dissociates into $H_3SiO_4^{2-}$ and $H_2SiO_4^{2-}$.

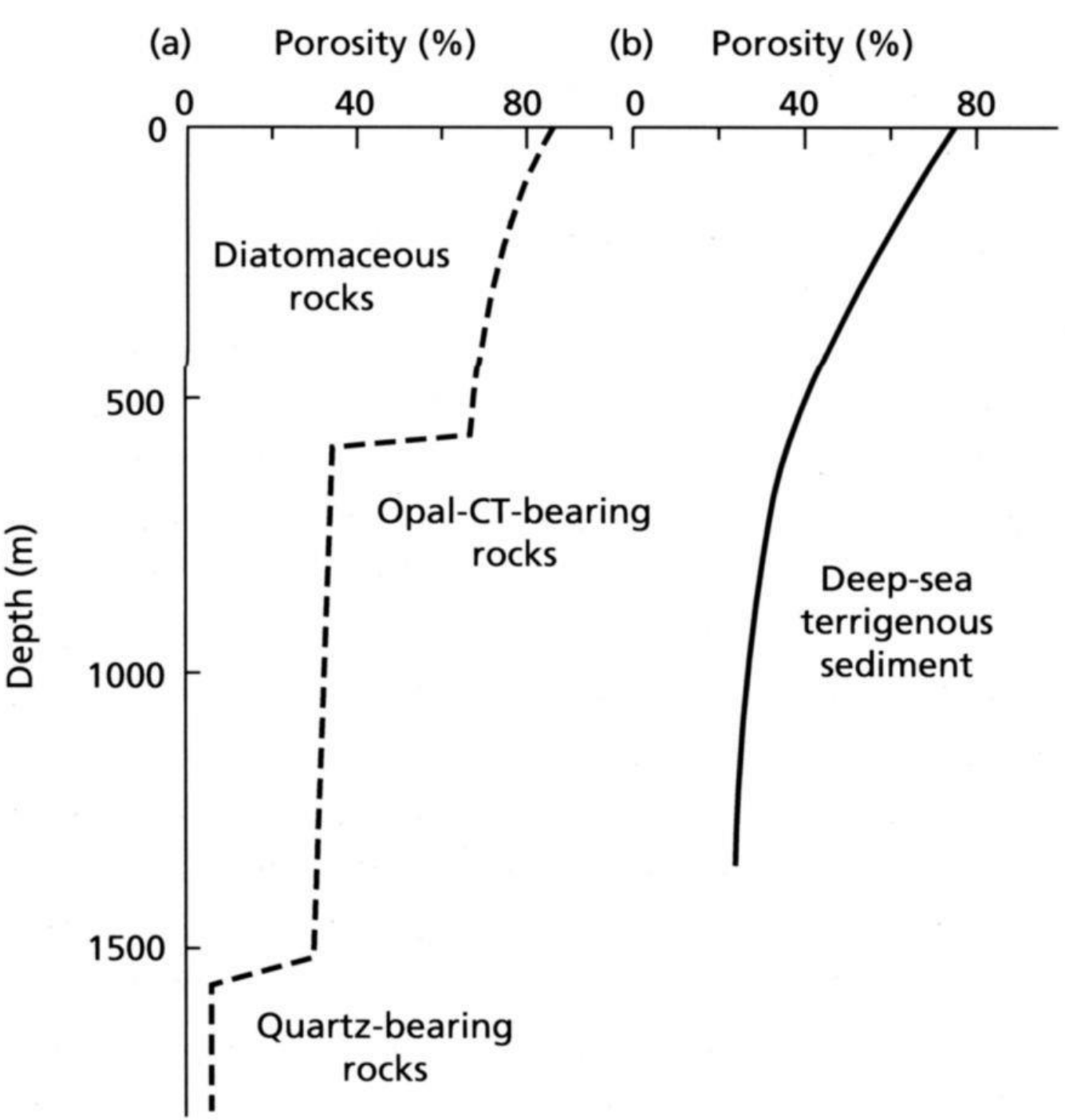
(a) Porosity (%)
0
40
80
0
(b) Porosity (%)
0
40
80
Depth (m)
500
1000
1500
Diatomaceous rocks
Opal-CT-bearing rocks
Quartz-bearing rocks
Deep-sea terrigenous sediment

Ferolity

zdroje & transport Fe, eH-pH pole stability Fe ox.-hox.

raná diageneze

glaukonit

granulární facie, impregnace, povlaky; autigenní Fe glaukonitický smektit, raně diag. Fe, K glaukonitická slída; řídící faktory : dostatek Fe, K, rovnováha mezi klastickým přínosem a vymýváním, nízká sedimentační rychlost (10^3 - 10^6 let)

feromanganové nodule

Table 6.1 The iron minerals of sedimentary rocks

Oxides	hematite α-Fe_2O_3
	magnetite Fe_3O_4
	goethite α-FeO.OH
	limonite $FeO.OH.nH_2O$
Carbonate	siderite $FeCO_3$
Silicates	berthierine $(Fe_4^{2+}\ Al_2)\ (Si_2Al_2)\ O_{10}\ (OH)_8$
	chamosite $(Fe_5^{2+}\ Al)\ (Si_3Al)\ O_{10}\ (OH)_8$
	greenalite $Fe_6^{2+}\ Si_4\ O_{10}\ (OH)_8$
	glauconite $KMg(FeAl)\ (SiO_3)_6.3H_2O$
Sulphides	pyrite FeS_2
	marcasite FeS_2

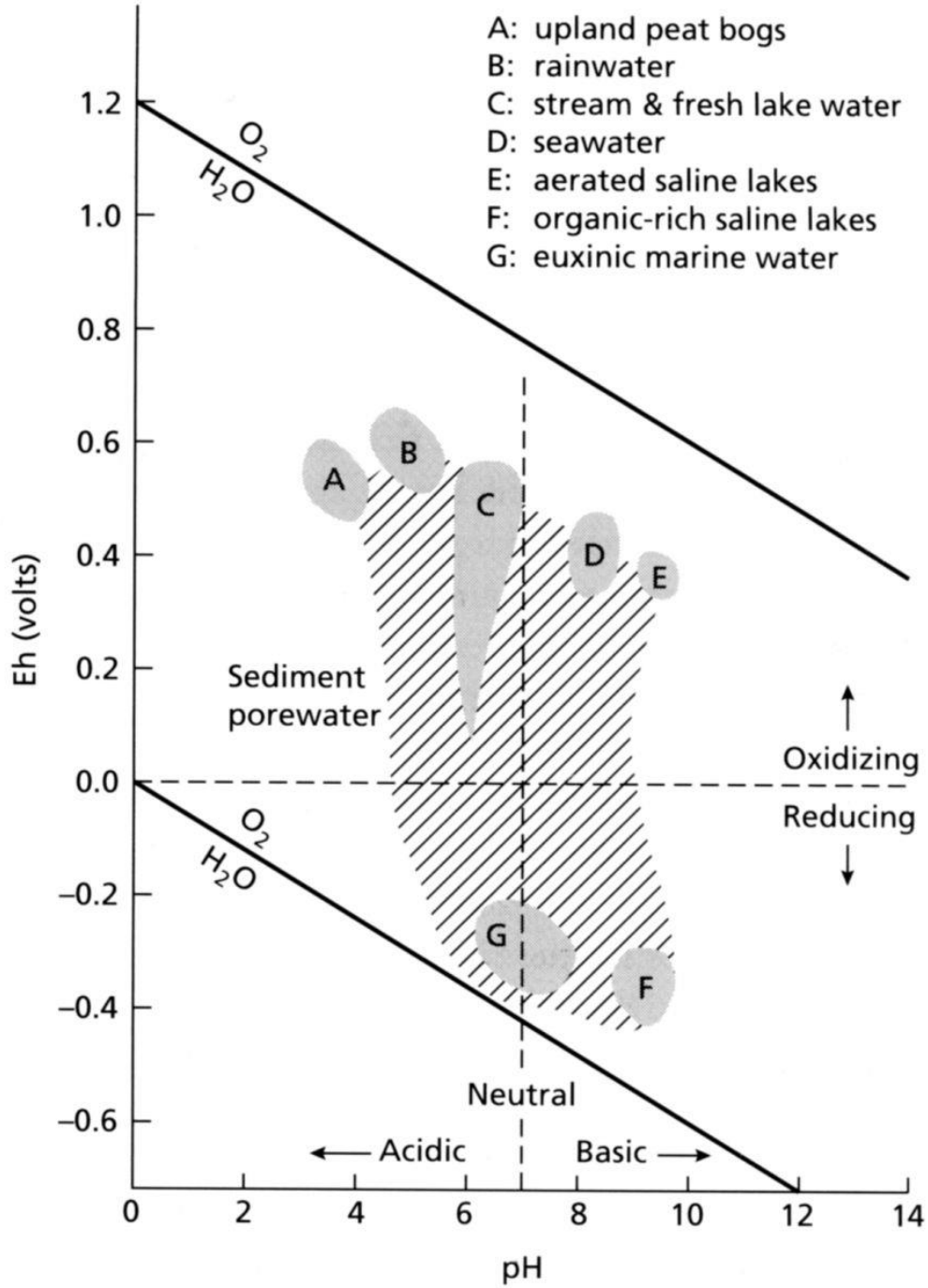
A: upland peat bogs
B: rainwater
C: stream & fresh lake water
D: seawater
E: aerated saline lakes
F: organic-rich saline lakes
G: euxinic marine water
1.2
1.0
0.8
0.6
0.4
0.2
0.0
−0.2
−0.4
−0.6
Eh (volts)
O2
H2O
O2
H2O
A
B
C
D
E
F
G
Sediment porewater
Oxidizing
Reducing
Neutral
Acidic
Basic
0
2
4
6
8
10
12
14
pH

Table 6.2 Geochemical classification of early diagenetic environments and the characteristic phases present. After Berner (1981)

Environment	Characteristic phases
Oxic	hematite, goethite, MnO_2-type minerals, no organic matter
Anoxic	
1 sulphidic	pyrite, marcasite, rhodochrosite, organic matter
2 non-sulphidic	
(a) post-oxic	glauconite, berthierine, no sulphide minerals, minor organic matter (also siderite, vivianite, rhodochrosite)
(b) methanic	siderite, vivianite, rhodochrosite, earlier formed sulphide minerals, organic matter

Table 6.3 Average concentration of Fe, Mn, Cu, Co and Ni (in percentages) of shallow- and deep-water sediments and ferromanganese nodules from three sea-floor settings. From Glasby (1977)

	Nearshore sediments	Deep-sea sediments, Atlantic	Seamount nodules	Abyssal nodules	Active ridge nodules
Fe	4.83	5.74	15.81	17.27	19.15
Mn	0.0850	0.3980	14.62	16.78	15.51
Cu	0.0048	0.0115	0.058	0.37	0.08
Co	0.0013	0.0039	1.15	0.256	0.40
Ni	0.0055	0.0079	0.351	0.54	0.31
Depth			1900 m	4500 m	2900 m

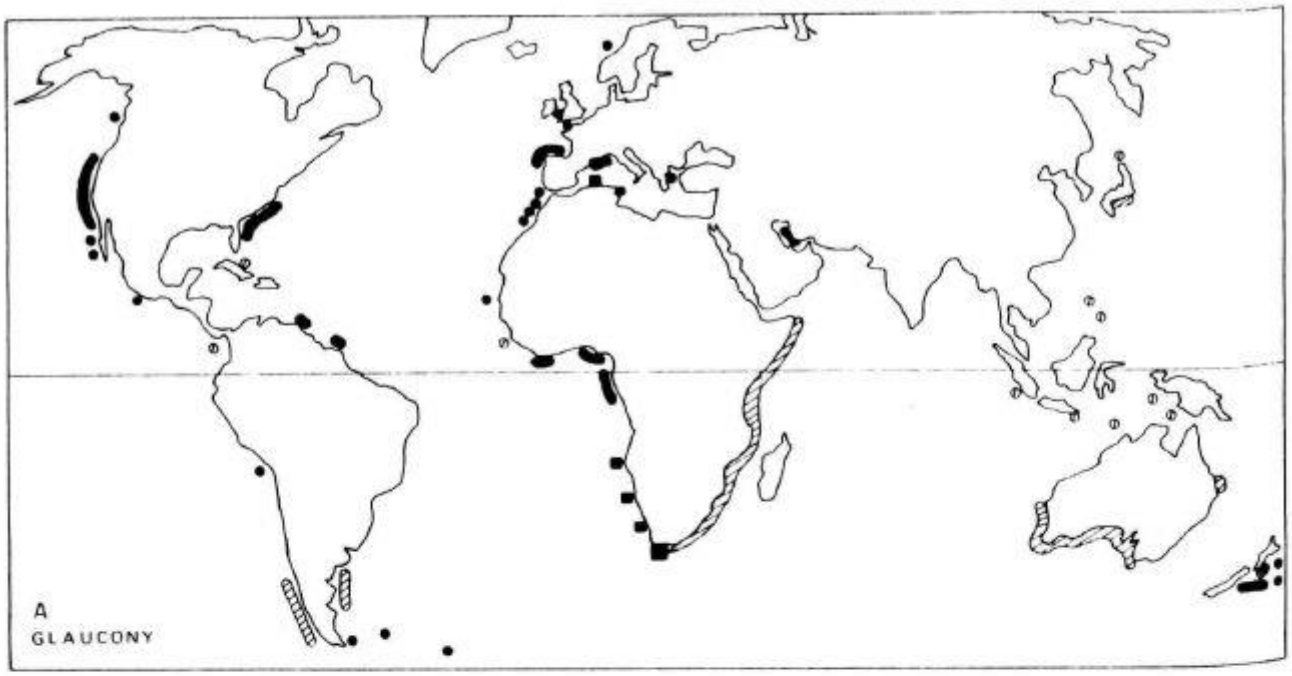
A
GLAUCONY

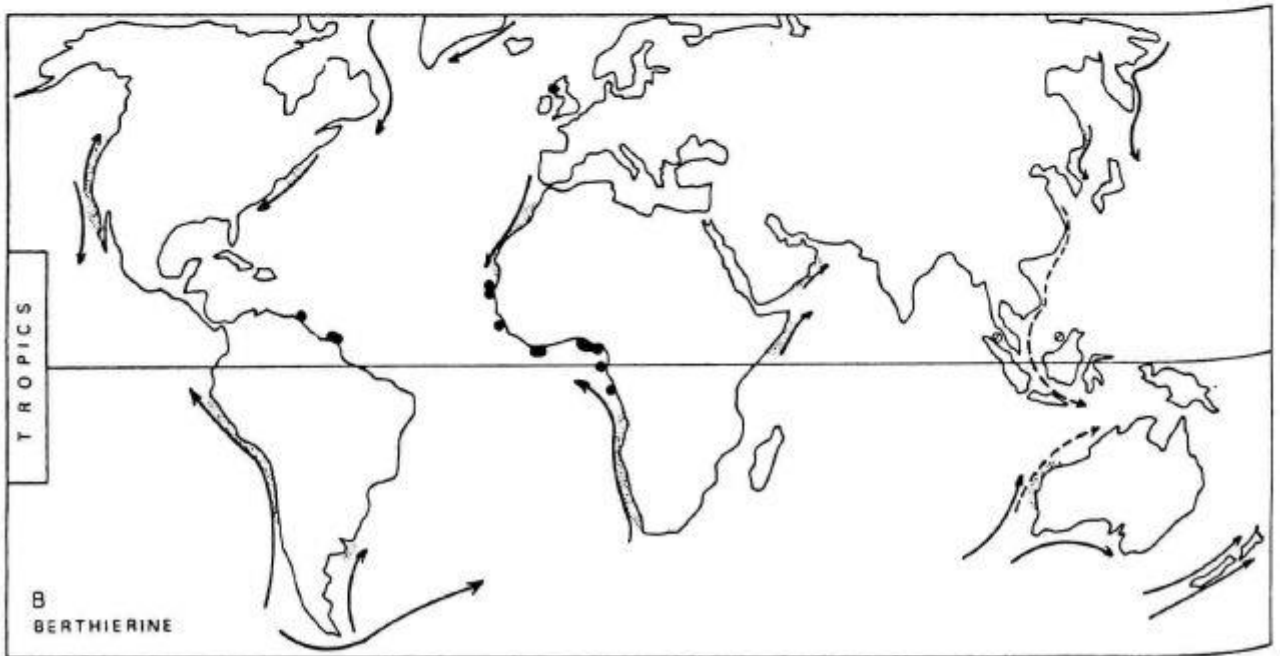
TROPICS
B
BERTHIERINE

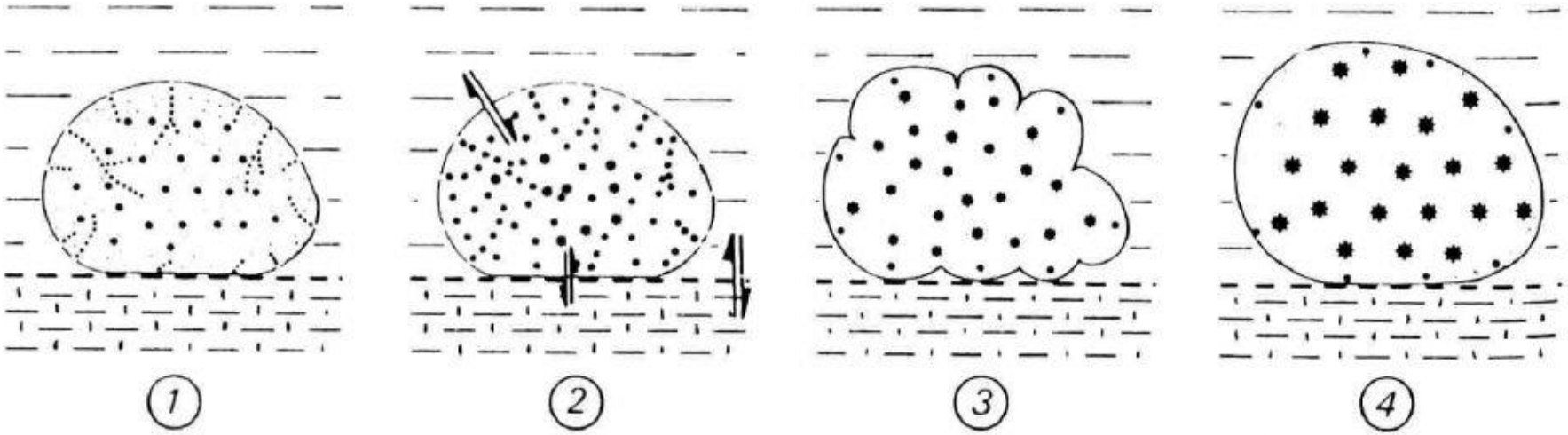

Fig. 12. Schematic representation of the evolution of a grain during glauconitization. Four stages from nascent (1) to highly-evolved (4) are selected from the continuum of changes observed in grains from the present shelf floor. Asterisks represent growth of glauconitic minerals. For discussion, see text.

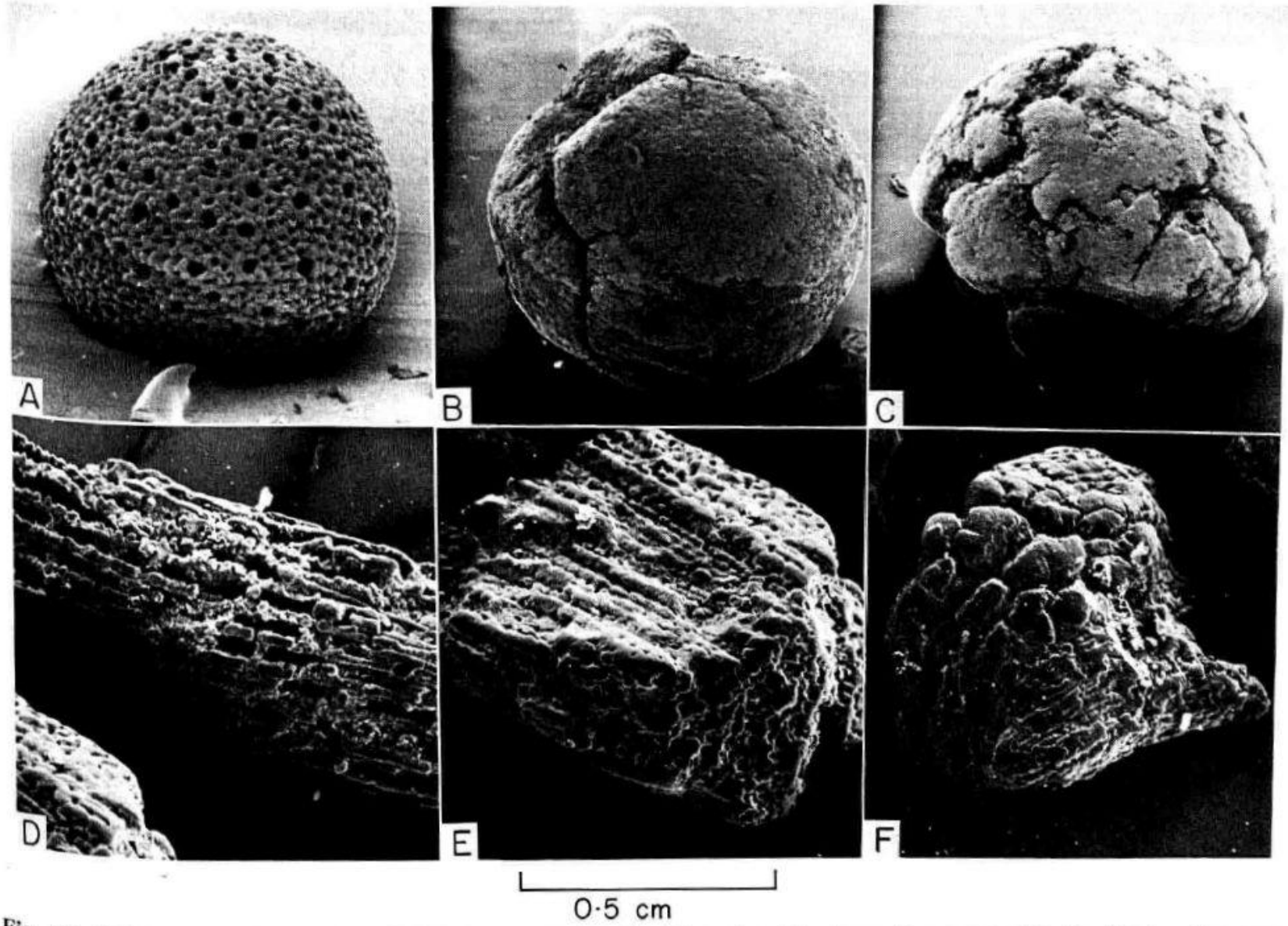

Fig. 15. SEM photomicrographs of Orbulina tests (A, B, C) and echinoderm fragments (D, E, F) showing progressive deformation during glauconitization. (A) Orbulina with pale green interior; (B) green mould with development of cracks; (C) dark green mould with large cracks leading eventually to splitting. Sequence (D) to (F) shows loss of original texture of echinoderm stereom during replacement by authigenic glauconitic crystals and development of a typical cracked grain.

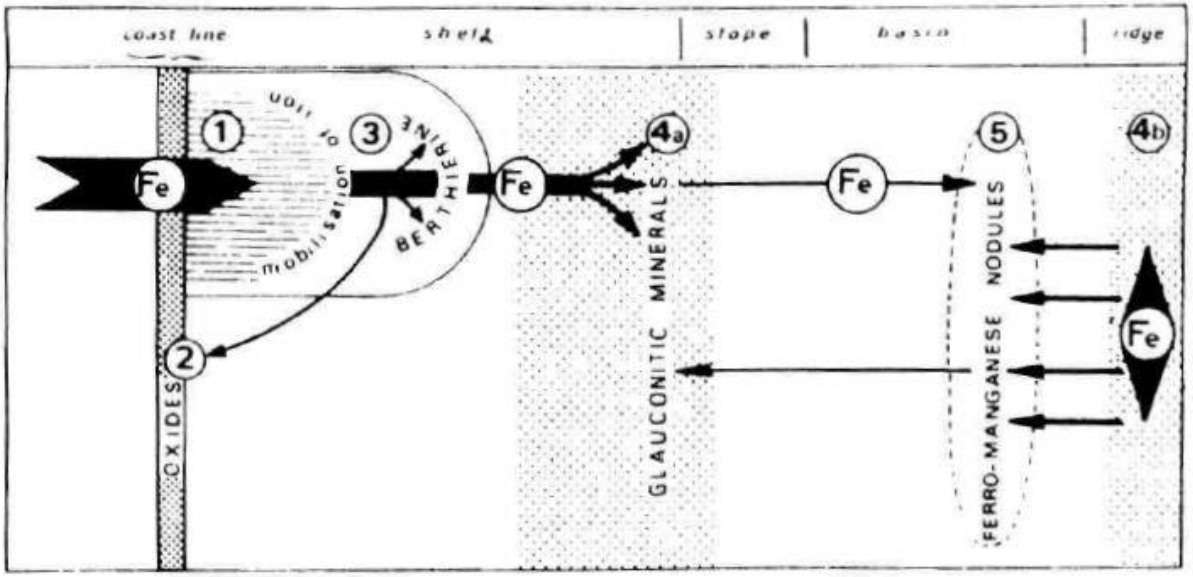

Fig. 19. Position of green sheet silicates in the geochemical path of iron in the sea. Zone 1, accumulation of detrital iron; zone 2, chemical precipitation of iron and oxidation of detrital iron minerals; zone 3, authigenic growth of berthierine; zones 4a, b, authigenic growth of glauconitic minerals; zone 5, growth of ferromanganese nodules. Modified from Odin (1975b).

hematitový ferolit

(c)

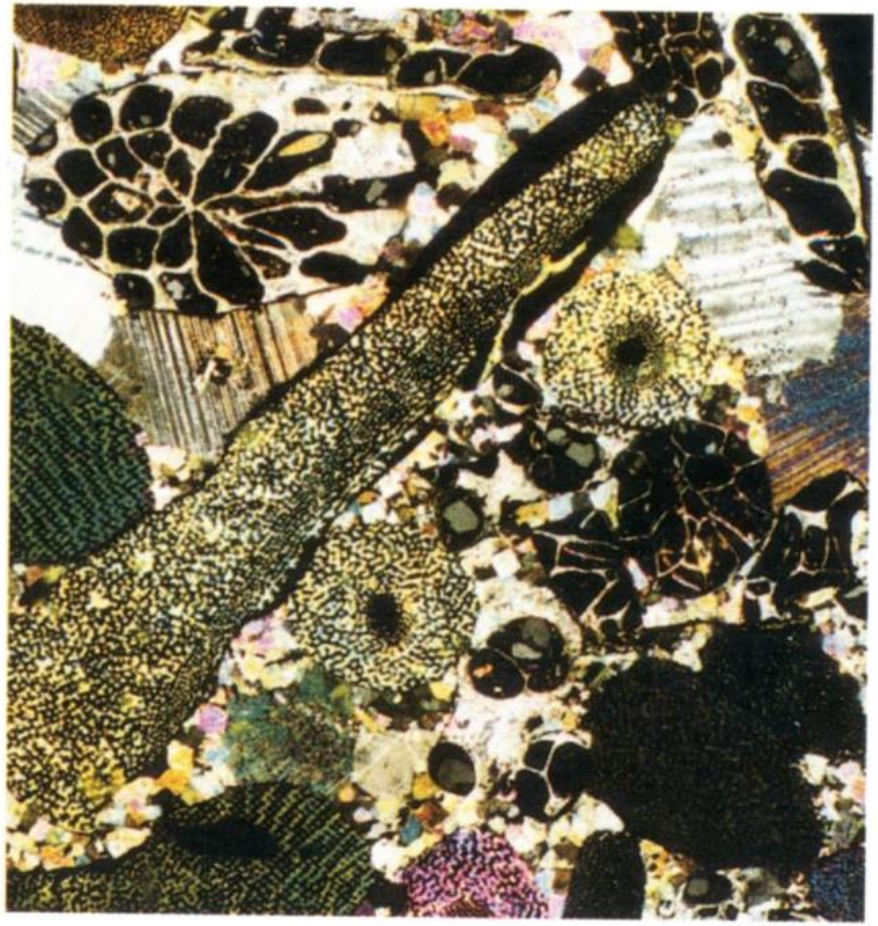

(d)

krinoidi, mechovky

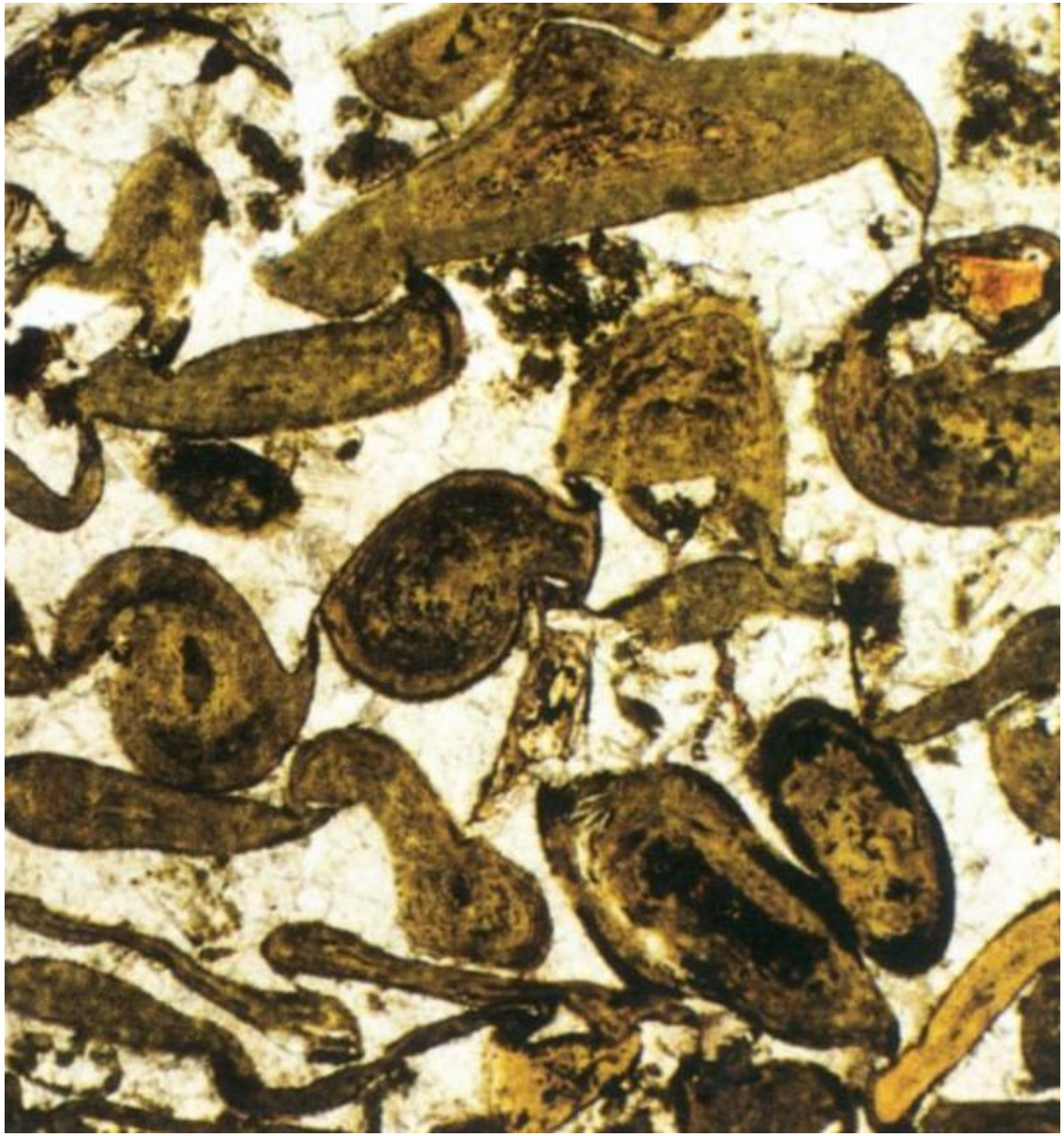

chamozitový ferolit
ooidy

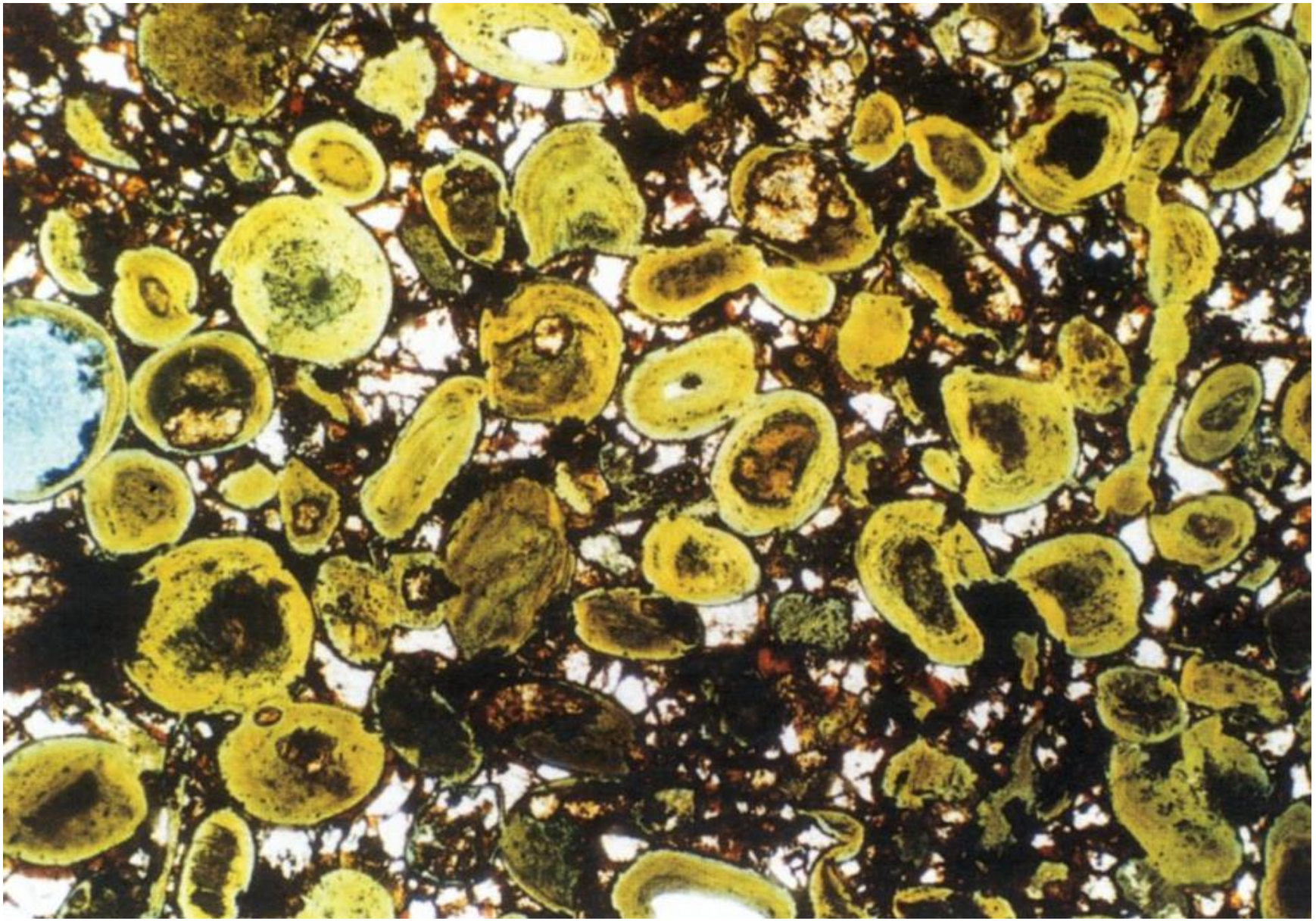

berthierit, chamozit, siderit, goethit

Fosfáty

mineralogie (karbonát fluorapatit - CFA, frankolit, alophan)

distribuce recentních výskytů

genetické modely marinních fosfátů - upwelling, ostrovy, atoly, podmořské hory, guyoty, epeirická prostředí

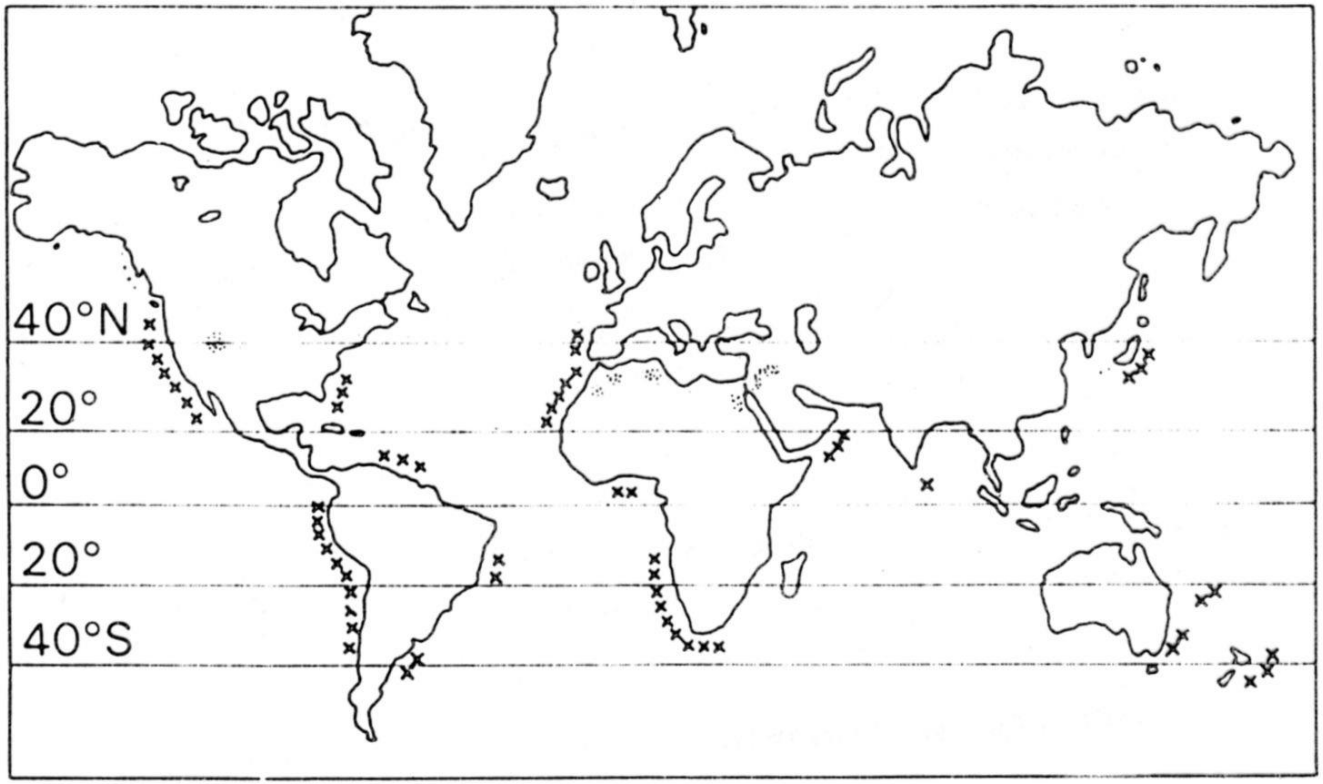

Fig. 7.1 Distribution of marine phosphorites, although in many cases the deposits are not actually forming at the present time. Also shown are the locations of the Permian Phosphoria Formation of northwestern USA and the Cretaceous–Tertiary phosphorites of the Middle East–North Africa.

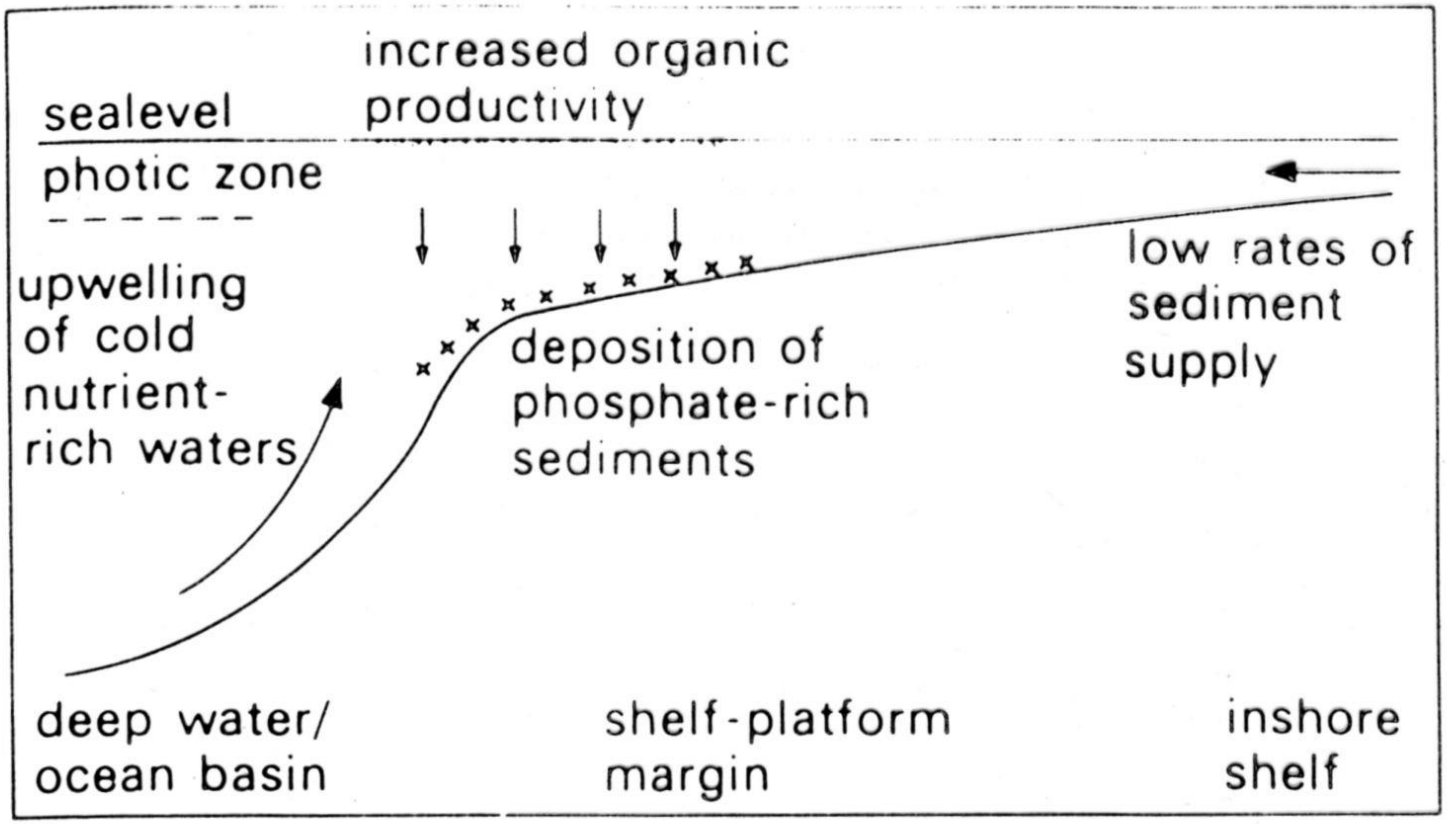

Fig. 7.2 Model for formation of marine phosphorites.

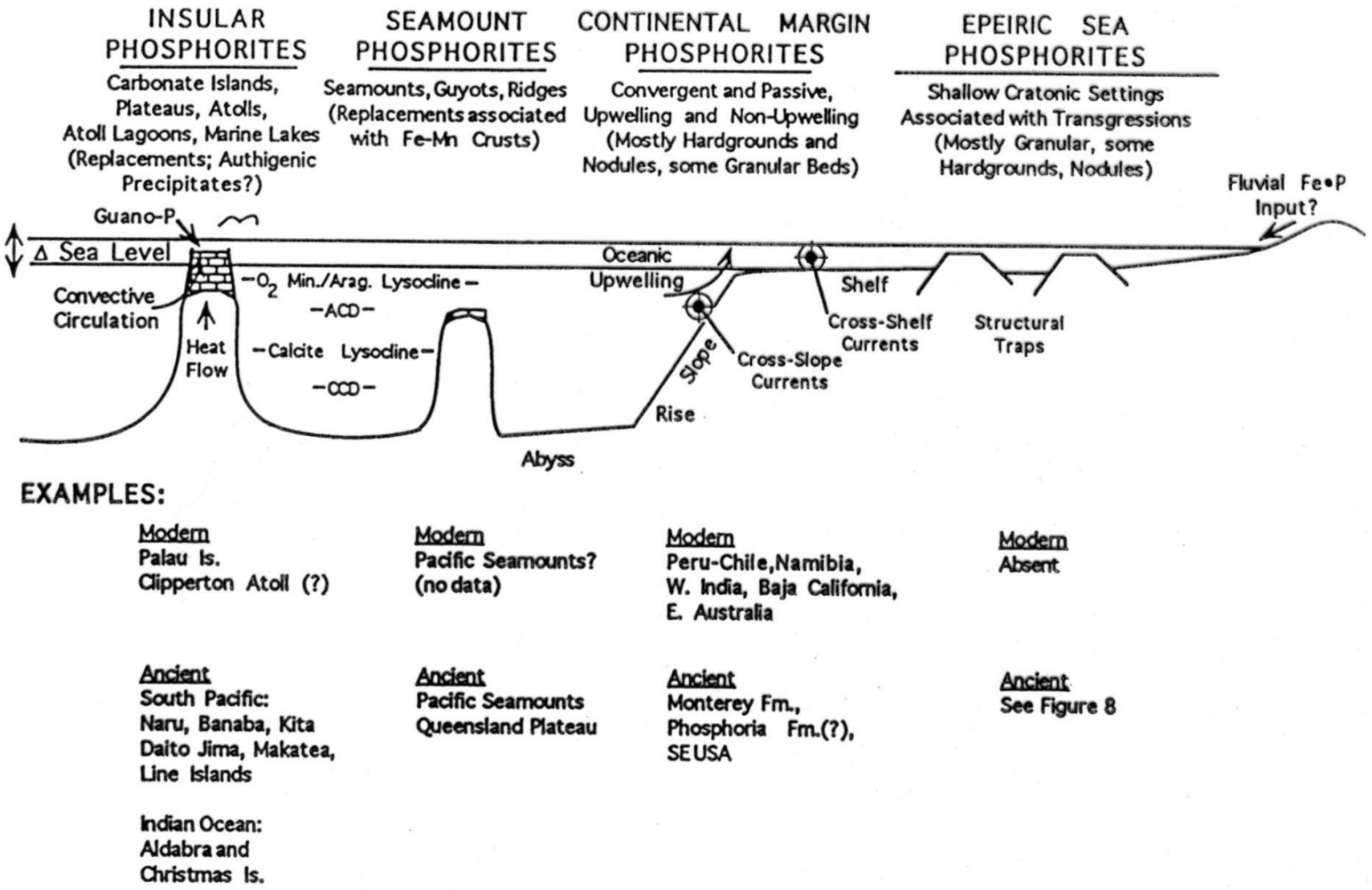

Fig. 1. Tectonic and oceanographic settings of marine phosphorites as derived from studies of the modern and ancient record.

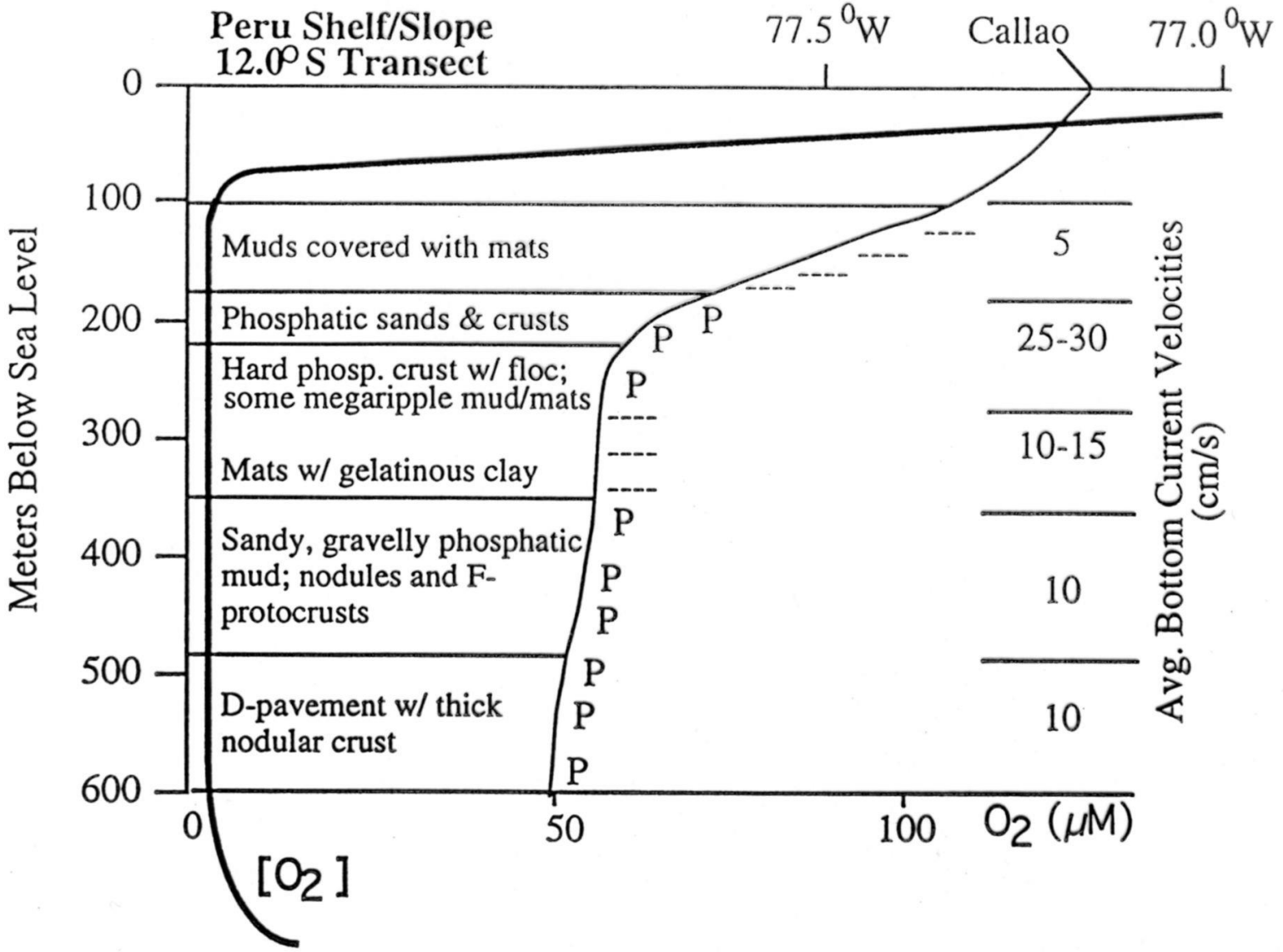
Peru Shelf/Slope
12.0° S Transect
77.5 °W
Callao
77.0 °W
0
100
200
300
400
500
600
Meters Below Sea Level
Muds covered with mats
Phosphatic sands & crusts
Hard phosp. crust w/ floc;
some megaripple mud/mats
Mats w/ gelatinous clay
Sandy, gravelly phosphatic
mud; nodules and F-
protocrusts
D-pavement w/ thick
nodular crust
P
5
25-30
10-15
10
10
Avg. Bottom Current Velocities
(cm/s)
0
50
100
O2 (μM)
[O2]

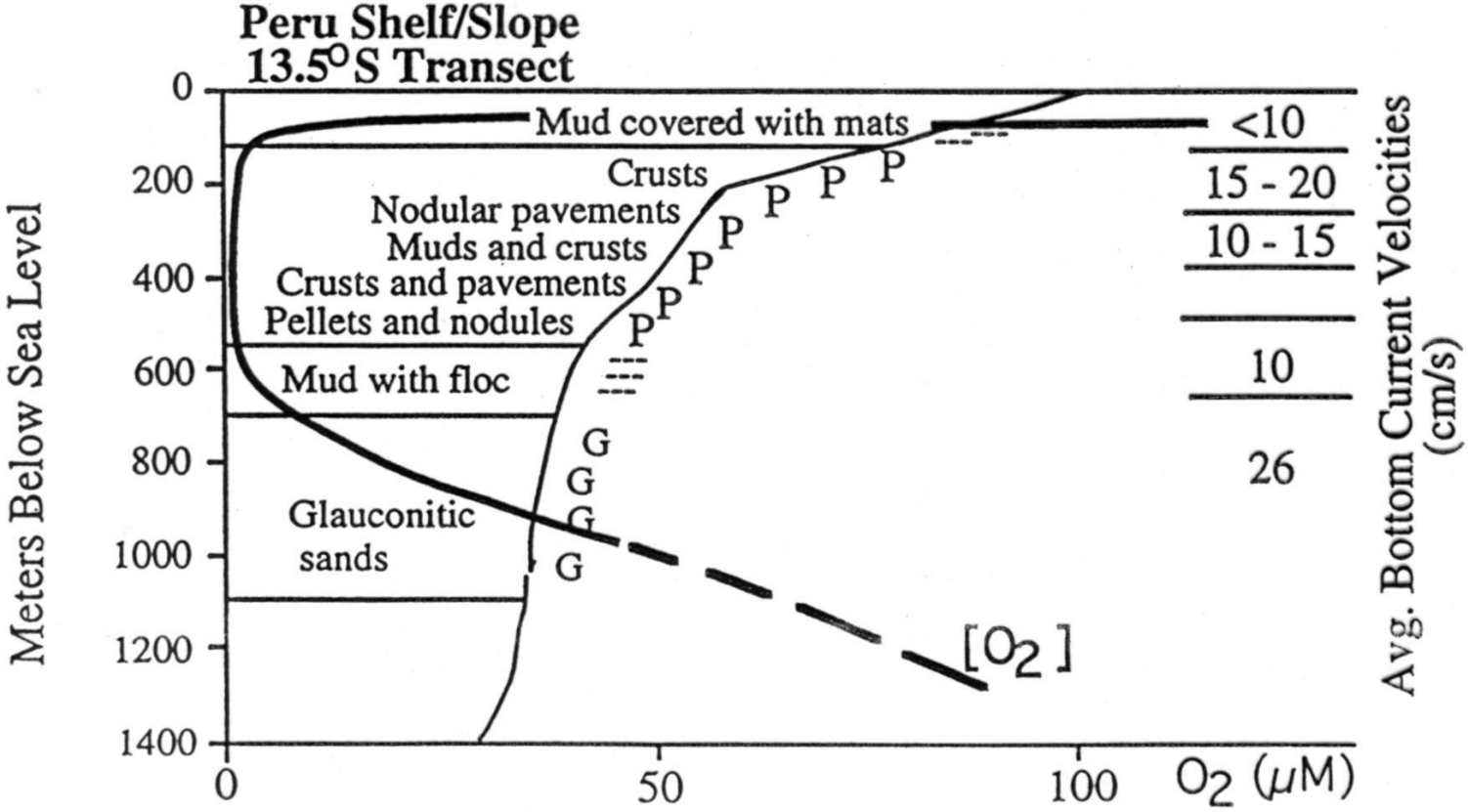

Fig. 5. Sediment and phosphorite distribution together with measured bottom current velocities (cm/s) and dissolved oxygen concentrations (μM) on the outer Peru shelf and upper slope at 12°S (top) and 13.5°S (bottom) (results from R/V *Seward Johnson,* 1992 cruise; unpublished). "P" represents distribution of phosphorite. Nodular hardground pavements and phosphatic sands occur in association with highest current velocities. Friable (F-phosphate) CFA-protocrusts occur between about 350 and 500 m. Glauconitic sands occur along the base of the oxygen minimum zone between 700 m and 1100 m at 13.5°S. Bacterial mats are sulfide-oxidizing *Thioploca* sp. After Glenn et al. 1994.

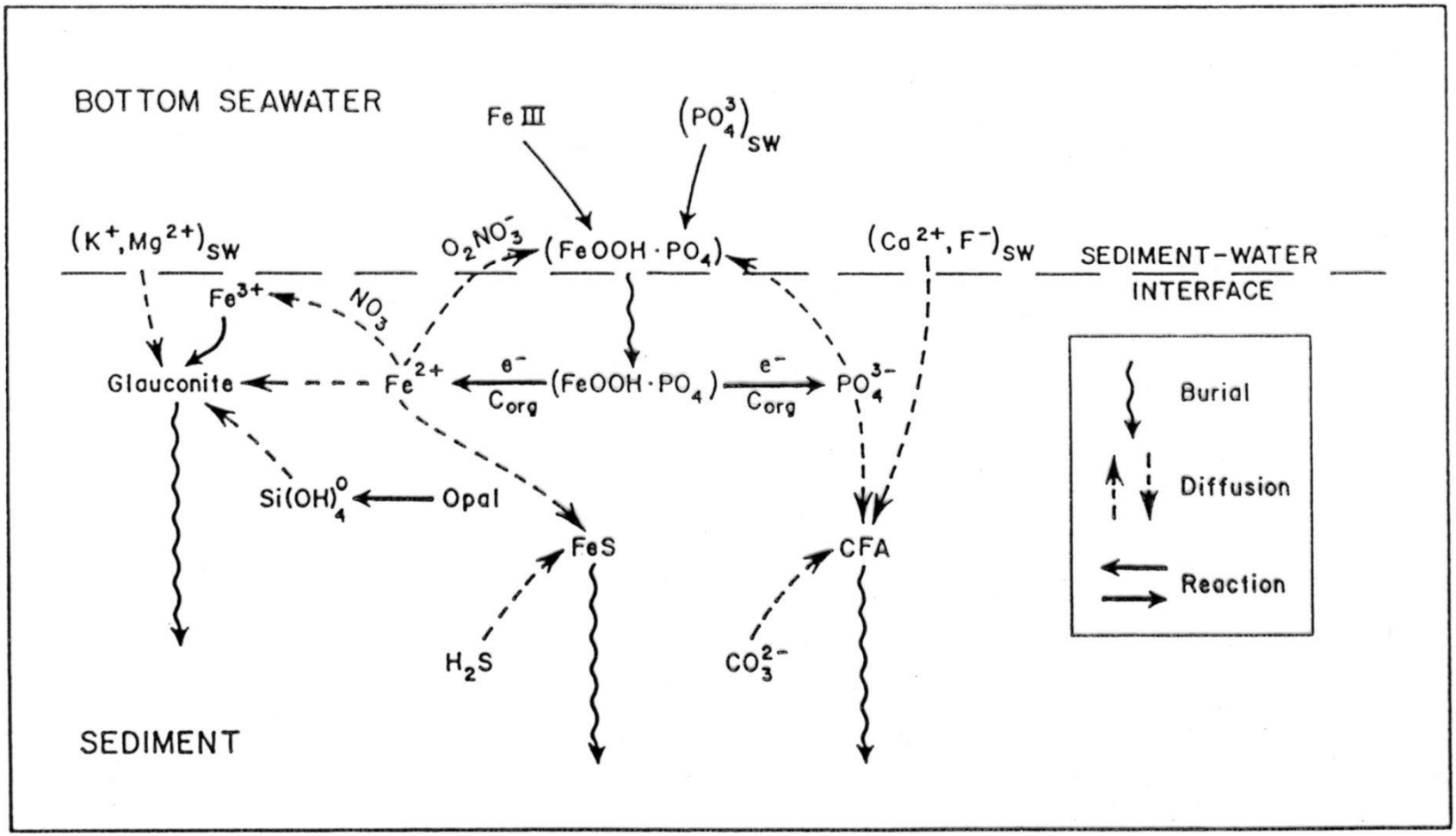

Fig. 6. Schematic diagram of iron redox-P cycle as postulated for Peru Margin sediments by Froelich et al. (1988). Iron hydroxyoxides sorb phosphate from bottom water and from upward diffusing pore water phosphate. Once reduced below the sediment-water interface these compounds release the sorbed phosphate to pore waters which is then precipitated. The reduced iron (Fe^{2+}) fluxes back to the more oxidizing environment of the bottom waters, where it may again sorb phosphate, or is precipitated in the sediments as a component of pyrite or glauconite. A somewhat similar mechanism has also been proposed for the modern sediments of the east Australian margin (see text). Reprinted with permission of Elsevier Science.

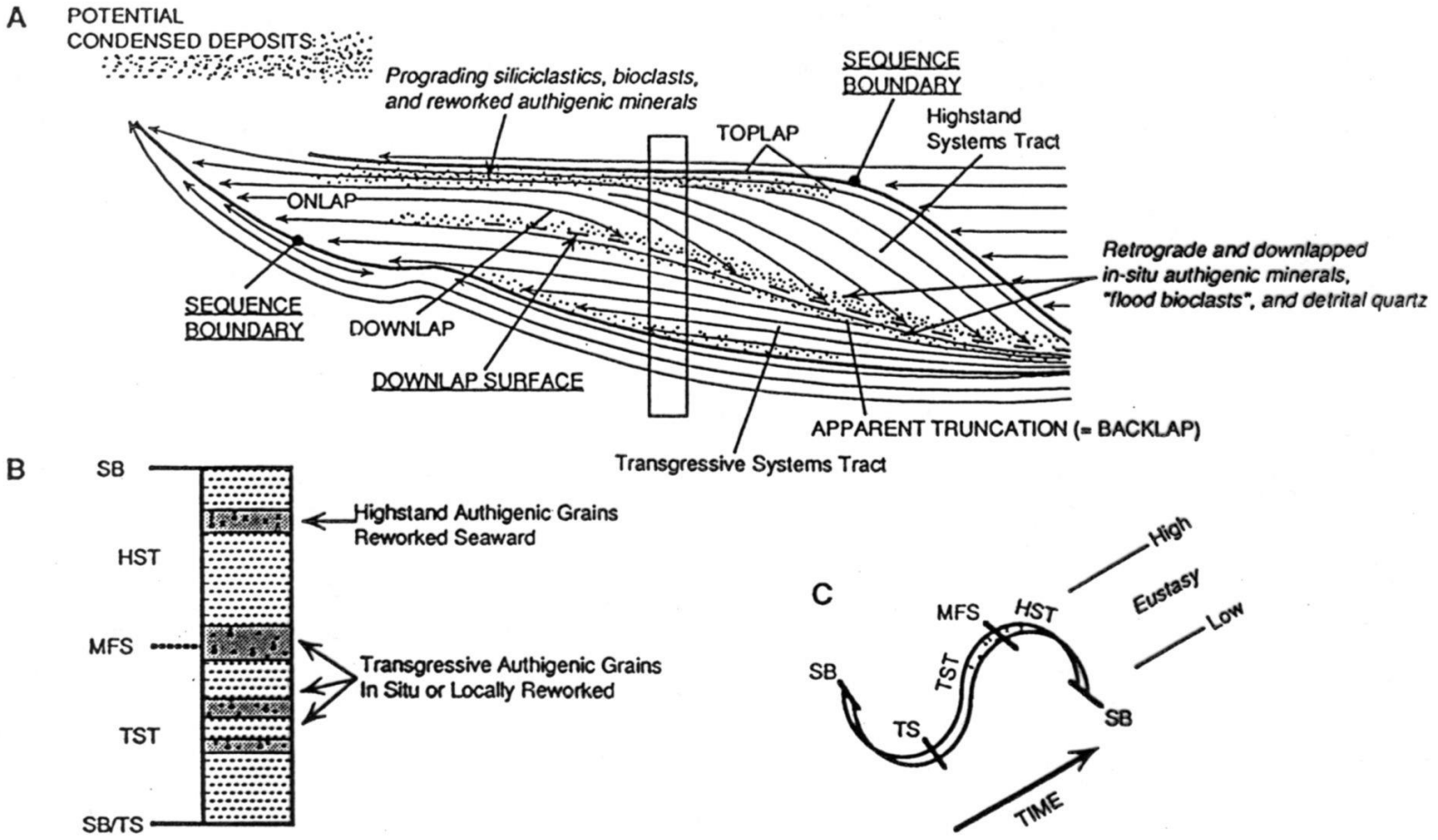

Fig. 10. Potential relationships between sequence stratigraphy, condensed sections and phosphorites. (**A**) Possible positions of sequence condensation within an idealized depositional sequence (stipples), (after Kidwell 1991). (**B**) Schematic illustration of the placement of non-reworked pristine authigenic phosphorite (and/or glauconite) and reworked phosphorite (and/or glauconite). Pristine phosphates may form within transgressive systems tracts and at the maximum flooding surface, whereas later phases are reworked seaward within highstand systems tracts. (**C**) The timing of systems tracts development with respect to one cycle of sea level change. LST = lowstand systems tract, TST = transgressive systems tract, HST = highstand systems tract, TS = transgressive surface, MFS = maximum flooding surface, SB = sequence boundary. Dots on the sea level curve represent locations of maximum phosphorite emplacement. After Glenn & Kronen 1993.

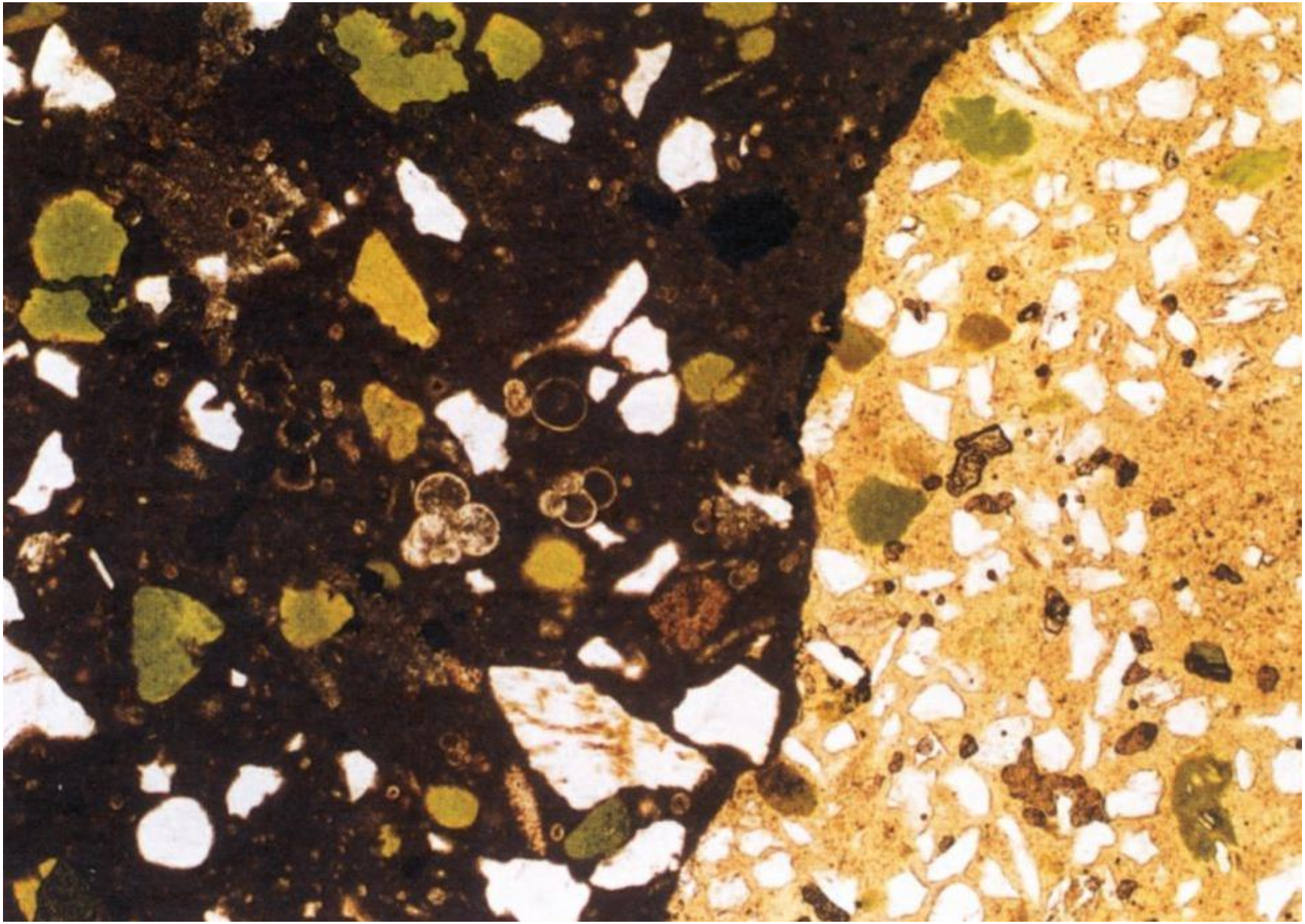

glaukonit, fosfát

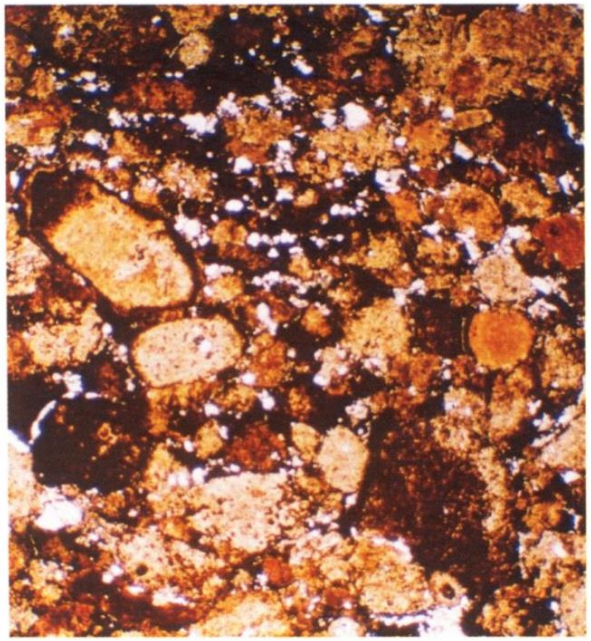

(c)

(d)

(e)

Evapority

chemismus mořské vody, minerální sukcese při izotermickém odpařování mořské vody

sedim. prostředí: subakvatické, subaerické - sabcha, okraj šelfu - laguna, salina, izolovaná pánev, playa

mikrostruktury sádrovec-anhydrit, halit, lakustrinní evapority

laterální a vertikální distribuce facií řízené rel. pohyby hladiny

diapirismus

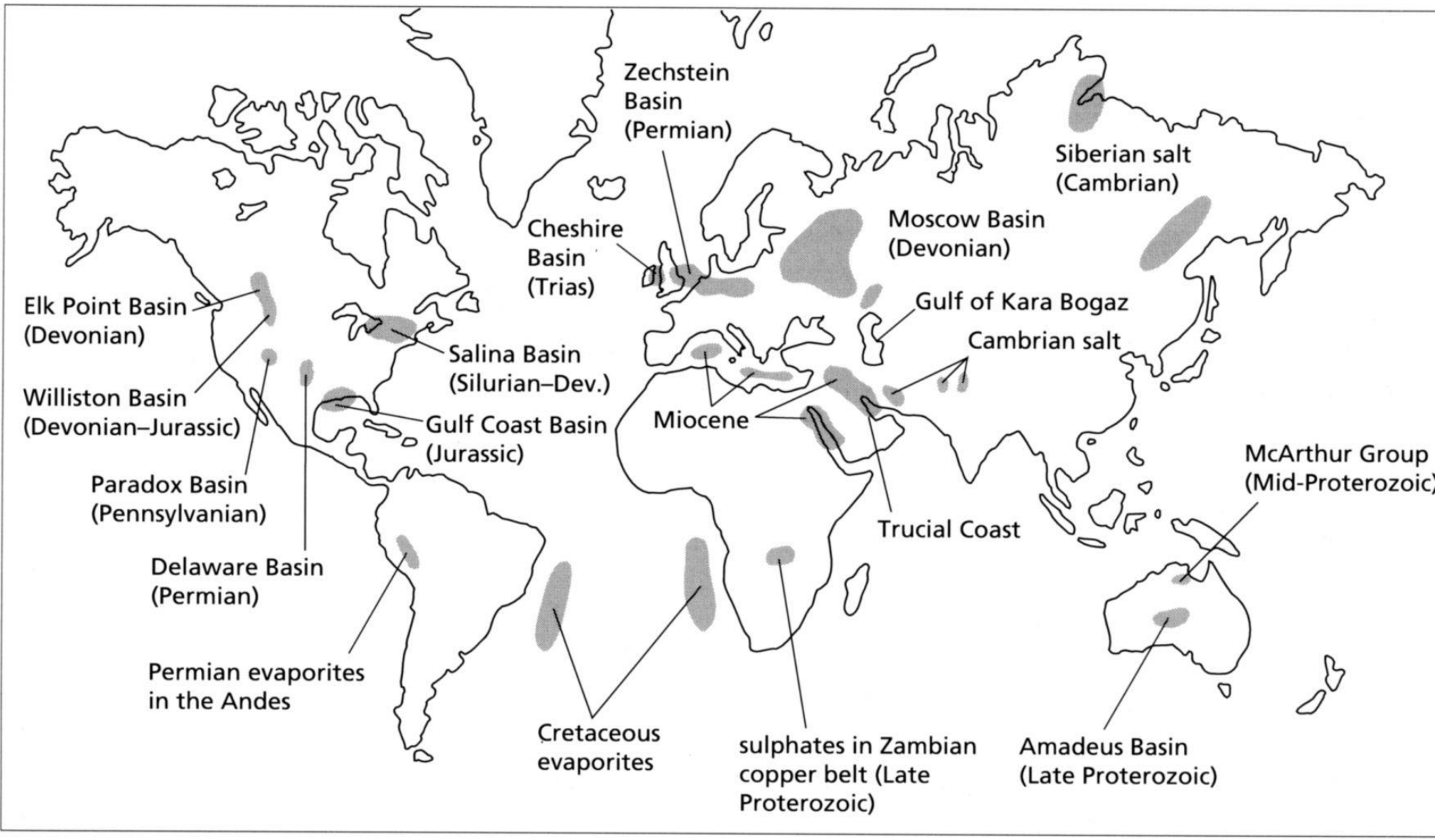
Zechstein Basin (Permian)
Siberian salt (Cambrian)
Moscow Basin (Devonian)
Cheshire Basin (Trias)
Elk Point Basin (Devonian)
Gulf of Kara Bogaz
Cambrian salt
Salina Basin (Silurian–Dev.)
Williston Basin (Devonian–Jurassic)
Gulf Coast Basin (Jurassic)
Miocene
McArthur Group (Mid-Proterozoic)
Paradox Basin (Pennsylvanian)
Trucial Coast
Delaware Basin (Permian)
Permian evaporites in the Andes
Cretaceous evaporites
sulphates in Zambian copper belt (Late Proterozoic)
Amadeus Basin (Late Proterozoic)

Table 5.1 The common marine and non-marine evaporite minerals

Marine evaporite minerals		Non-marine evaporite minerals	
halite	$NaCl$	halite, gypsum, anhydrite	
sylvite	KCl	epsomite	$MgSO_4 . 7H_2O$
carnallite	$KMgCl_3 . 6H_2O$	trona	$Na_2CO_3 . NaHCO_3 . 2H_2O$
kainite	$KMgClSO_4 . 3H_2O$	mirabilite	$Na_2SO_4 . 10H_2O$
anhydrite	$CaSO_4$	thenardite	$NaSO_4$
gypsum	$CaSO_4 . 2H_2O$	bloedite	$Na_2SO_4 . MgSO_4 . 4H_2O$
polyhalite	$K_2MgCa_2(SO_4)_4 . 2H_2O$	gaylussite	$Na_2CO_3 . CaCO_3 . 5H_2O$
kieserite	$MgSO_4 . H_2O$	glauberite	$CaSO_4 . Na_2SO_4$

Table 5.2 The composition of sea water expressed in parts per million and percentage of total dissolved species. For comparison, the composition of world average river water, with a salinity of around 120 ppm is also given. Data from Krauskopf (1979)

	Seawater		
Dissolved species	ppm	% of total	River water
Cl^-	18 000	55.05	7.8
Na^+	10 770	30.61	6.3
SO_4^{2-}	2715	7.68	11.2
Mg^{2+}	1290	3.69	4.1
Ca^{2+}	412	1.16	15.0
K^+	380	1.10	2.3
HCO_3^-	140	0.41	58.4
Br^-	67	0.19	0.02
H_3BO_3	26	0.07	0.1
Sr^{2+}	8	0.03	0.09
F^-	1.3	0.005	0.09
H_4SiO_4	1	0.004	13.1

Tab. 19

Čtyři základní stádia krystalizace solí při izotermickém odpařování mořské vody

stádium	hlavní produkt krystalizace	násobek koncentrace rozpuštěných látek	snížení objemu solanky
I.	karbonáty Ca	1 - 3,35	0 - 1/5
II.	sulfáty (hlavně sádrovec a anhydrit)	3,35 - 10,96	1/5 - 1/10
III.	chloridy Na (hlavně helit + zbytkové sulfáty)	10,96 - 60,43	1/10 - 1/20
IV.	chloridy a sulfáty K a Mg (+ malé množství halitu a Ca sulfátu)	nad 60,43	nad 1/20

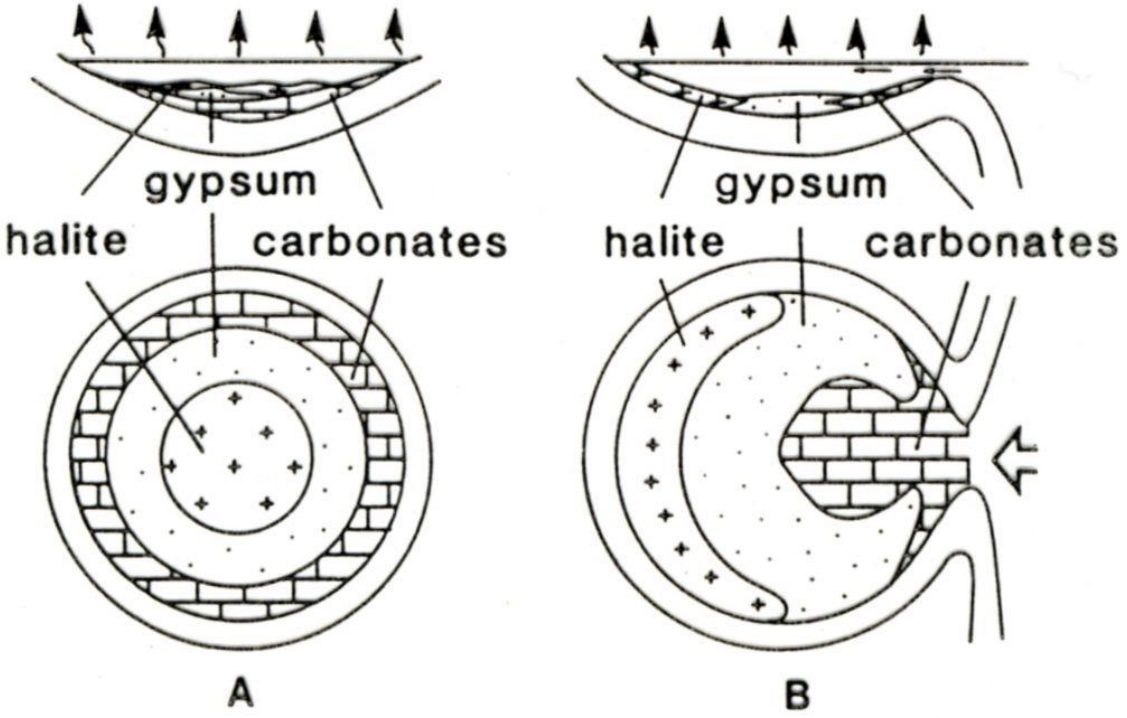

Fig. 5.20 Broad patterns of evaporite facies. A, Bullseye pattern, with the most soluble salts in the basin centre, typical of completely enclosed basins. B, Tear-drop pattern, typical of restricted basins with near-permanent connection to the open ocean, where the most soluble salts occur farthest away form the basin entrance. After Schmaltz (1969).

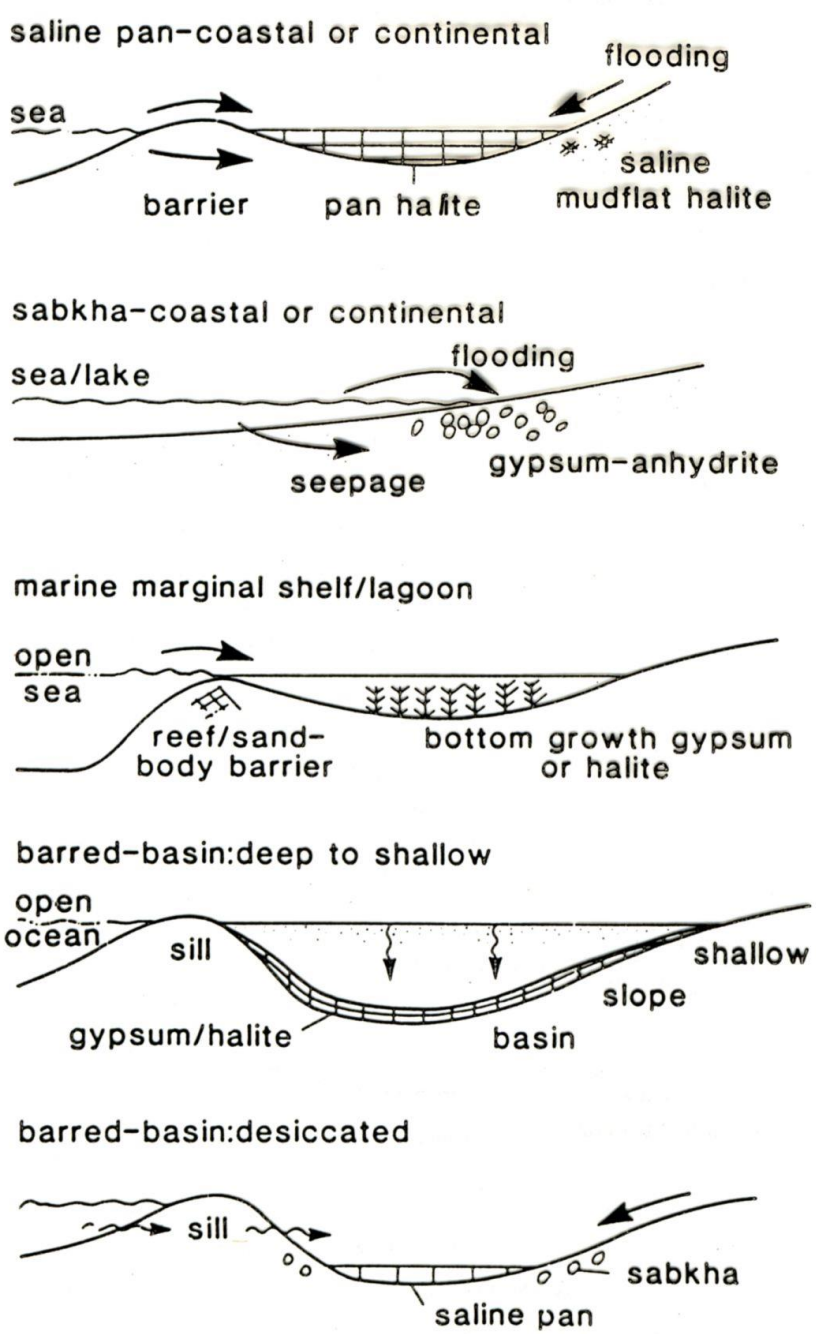

Fig. 5.2 Principal depositional environments of evaporites.

Table 5.3 The theoretical thickness of salts precipitated from sea water compared with the thickness of these salts in the Permian Zechstein of Germany, expressed as 100 m of precipitated evaporite. Note that there is much more $CaSO_4$ and much less Mg and K salts in the Zechstein deposits compared with the theoretical. Also shown is the approximate thickness of the various salts produced by the evaporation of a column of sea water 1000 m high. After Borchert & Muir (1964)

Component	Mineral	Thickness in 100 m of evaporite		Salt thickness from 1000 m of sea water
		from sea water	Permian Zechstein	
$MgCl_2$	in bischofite and carnallite	9.4	0.5	1.5
KCl	sylvite and in carnallite	2.6	1.5	0.4
$MgSO_4$	in kieserite	5.7	1.0	1.0
NaCl	halite	78	78	12.9
$CaSO_4$	anhydrite	3.6	16	0.6
$CaCO_3$	calcite	0.4	3	0.1
$CaMg(CO_3)_2$	dolomite			

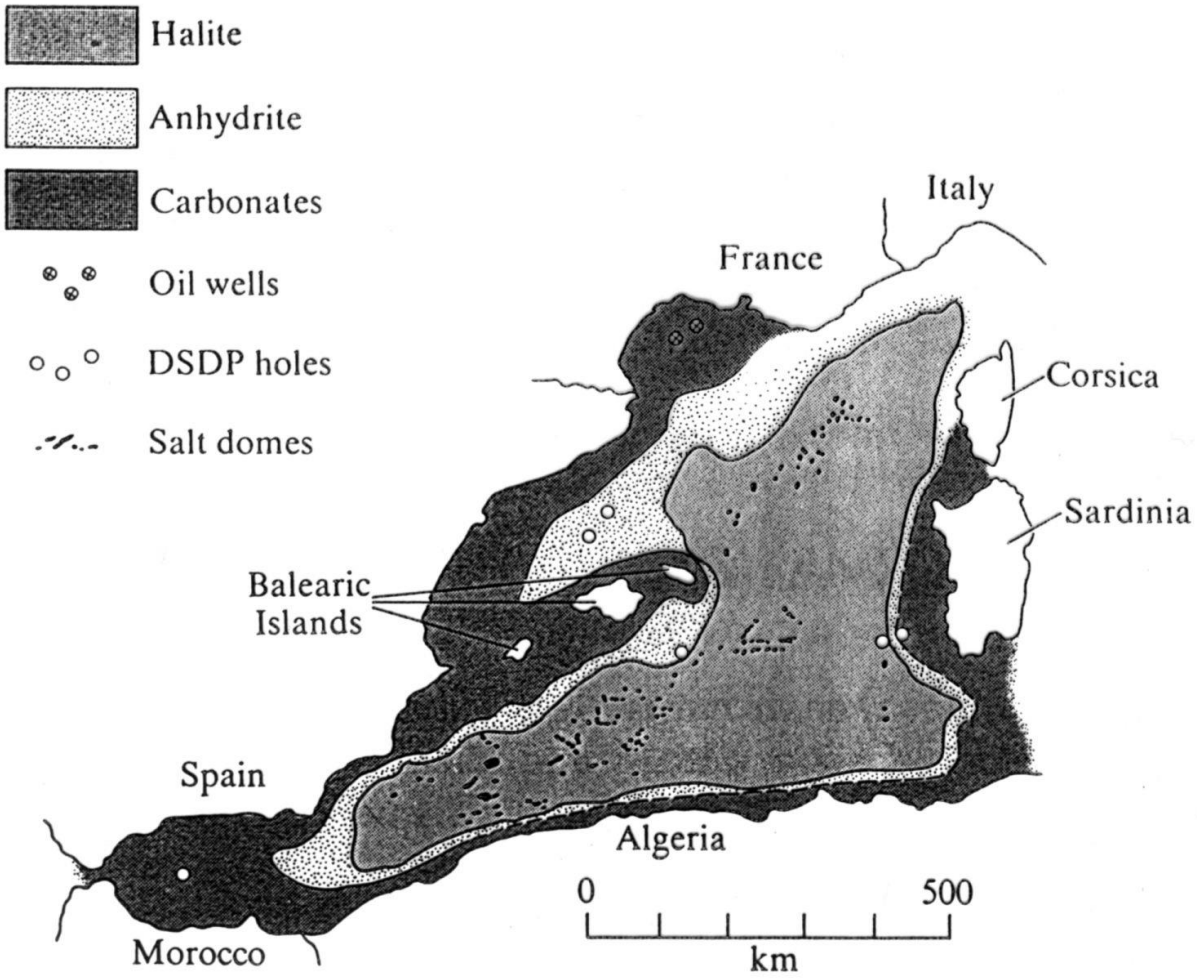

Figure 10-21
Evaporite distribution in Miocene rocks of Balearic Basin of Mediterranean Sea immediately east of Strait of Gibraltar. Balearic was one of several topographically low salt pans on floor of desiccated Mediterranean. Potash salts (not shown) occur in middle of halite area. [Hsü, 1972, *Earth-Science Rev., 8,* p. 390.]

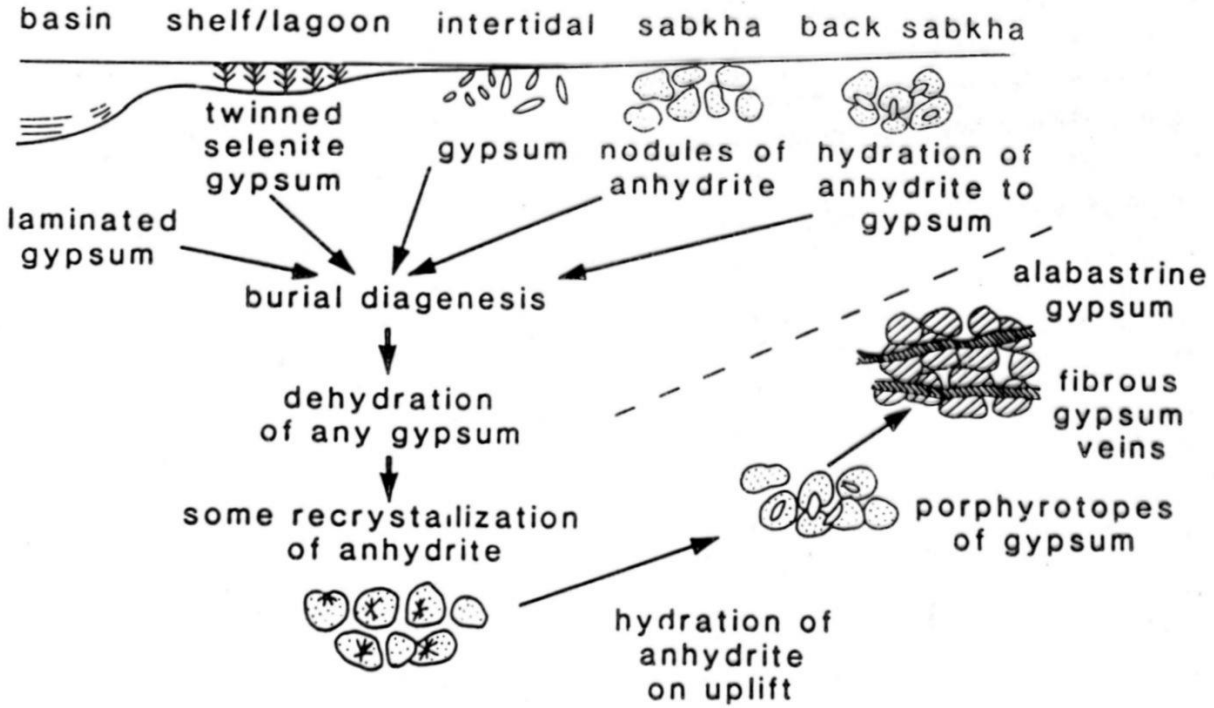

Fig. 5.3 The 'gypsum-anhydrite cycle showing mineral and textural changes from the surface, into the subsurface and on uplift.

Table 5.4 The water chemistry of five salt lakes (in ppm). The main point to note is the great variability in the relative concentrations of the constituents between lakes

	Dead Sea	Great Salt Lake, Utah	Mono Lake, California	Borax Lake, California	Gulf of Kara, Bogaz, USSR
Cl^-	208 020	112 900	15 100	5945	142 500
SO_4^{2-}	540	13 590	7530	22	46 900
HCO_3^-	240	180	26 430	6668	—
Na^+	34 940	67 500	21 400	6199	81 200
K^+	7560	3380	1120	322	
Ca^{2+}	15 800	330	11	nil	4900
Mg^{2+}	41 960	5620	32	30.7	19 900
Total salinity	315 040	203 490	71 900	>19 400	>293 000

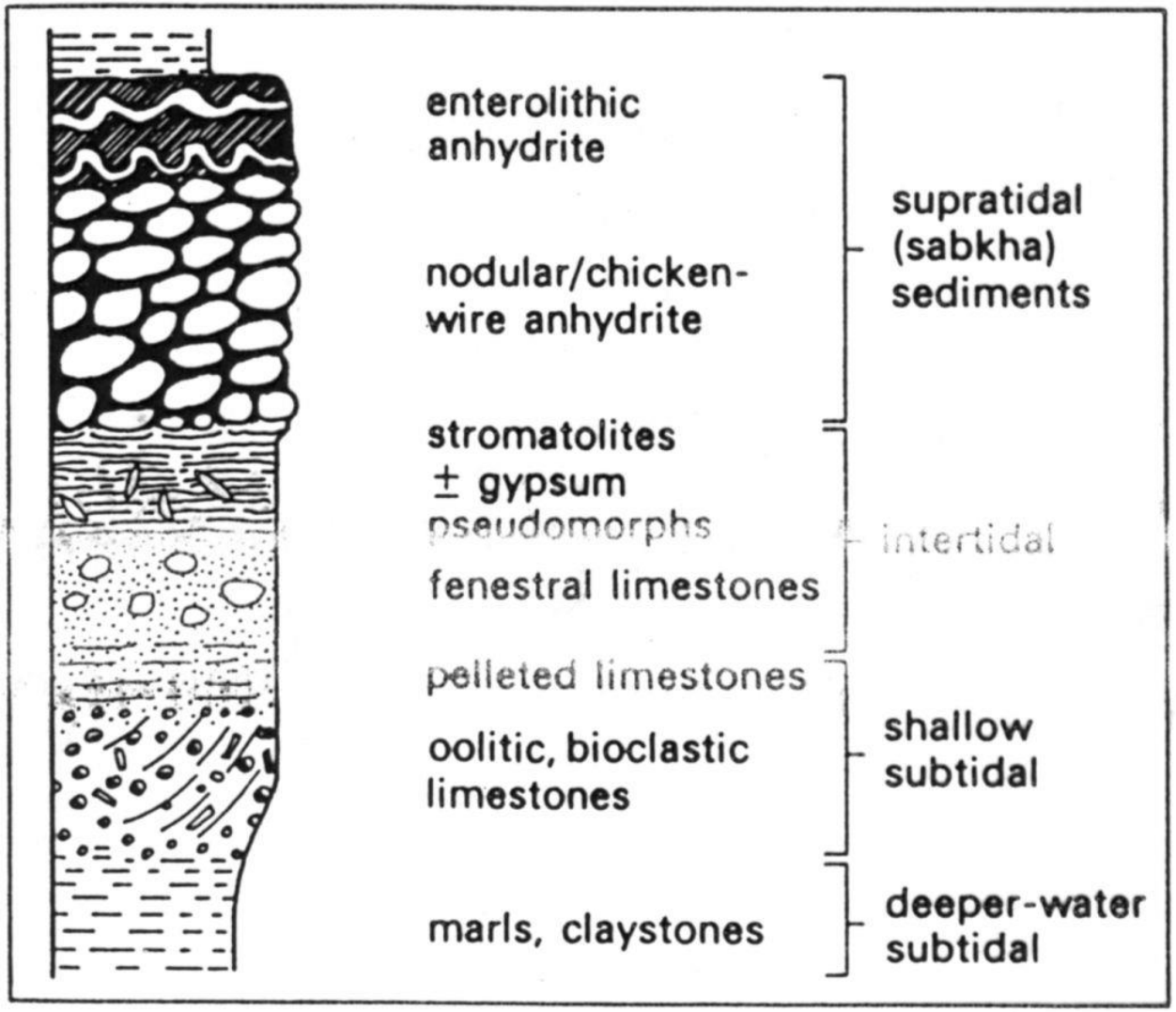

Fig. 5.17 A sabkha cycle. Such cycles typically range from several to several tens of metres in thickness.

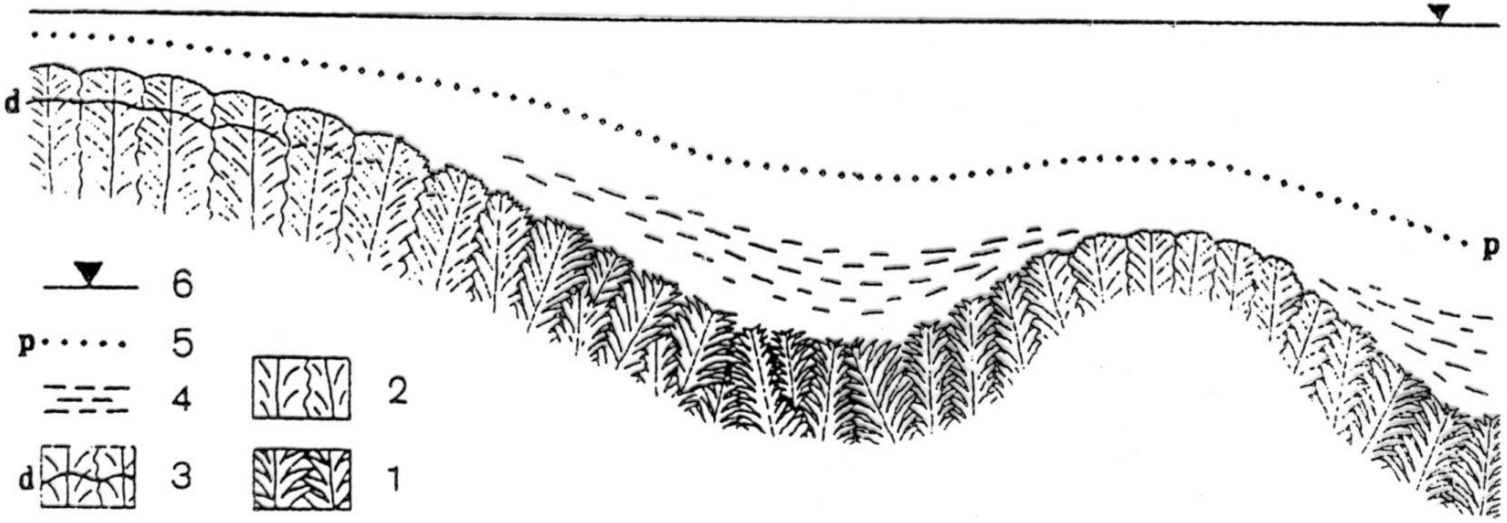

Fig. 7 *Model środowiska sedymentacji gipsów szklicowych o budowie palisadowej (subfacje 2a i 2b)*
1 - kryształy o budowie szkieletowej (subfacja 2a), 2 - kryształy o budowie masywnej (subfacja 2b), 3 - powierzchnie rozpuszczania (d), 4 - zawiesina ilasta, 5 - pyknoklina (p), 6 - poziom wody

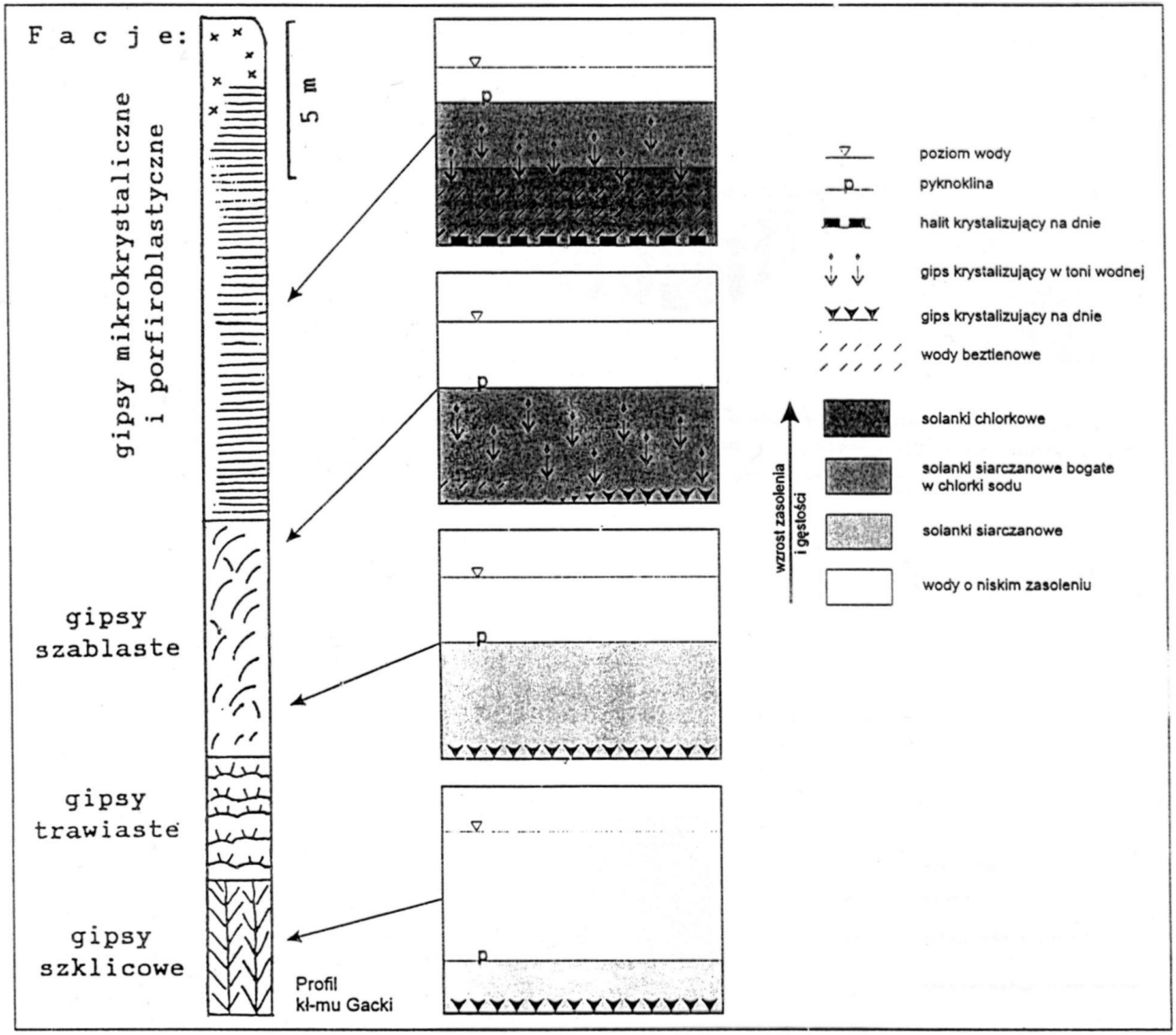

Fig. 27 *Ewolucja składu i struktury wód basenu ewaporacyjnego*

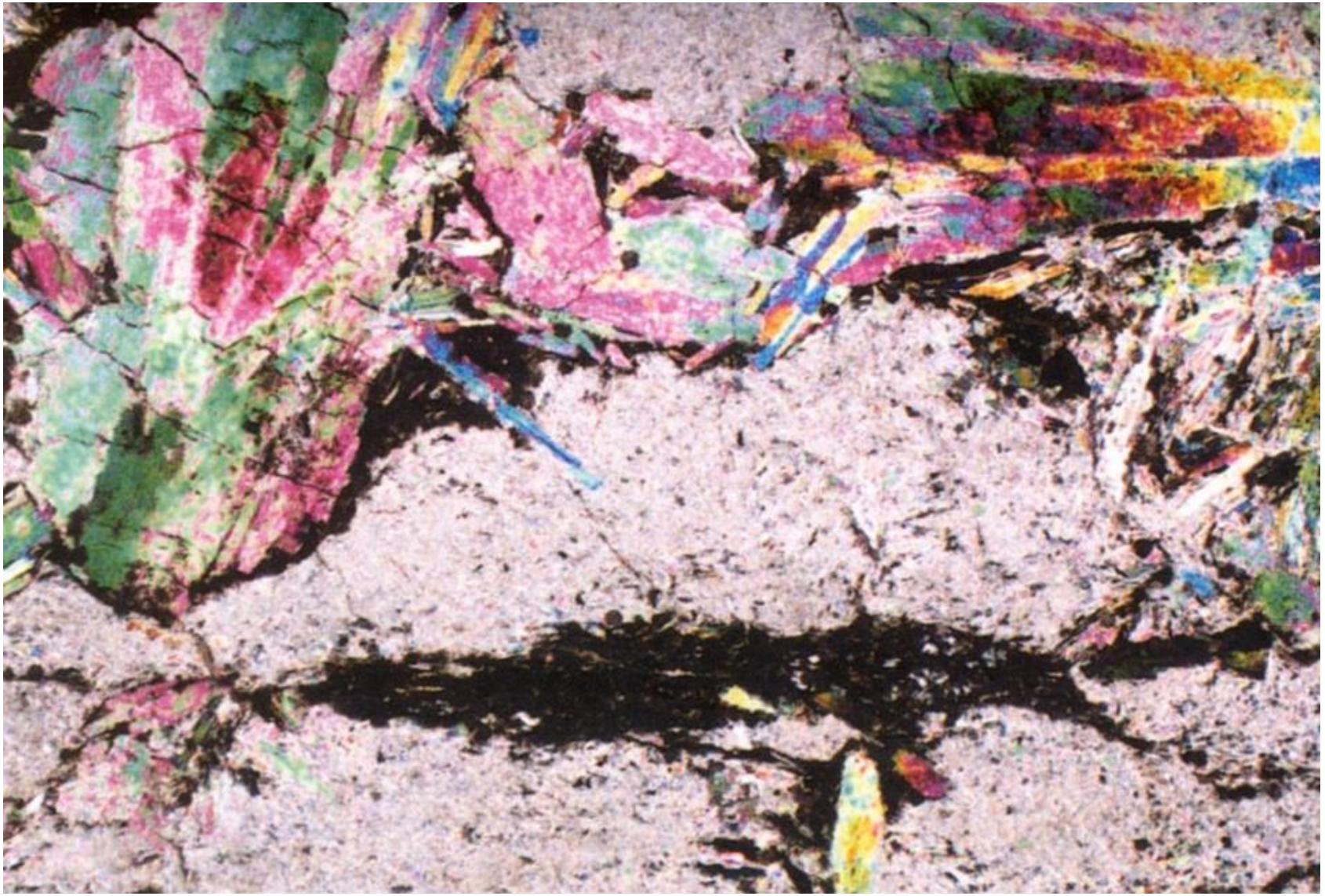

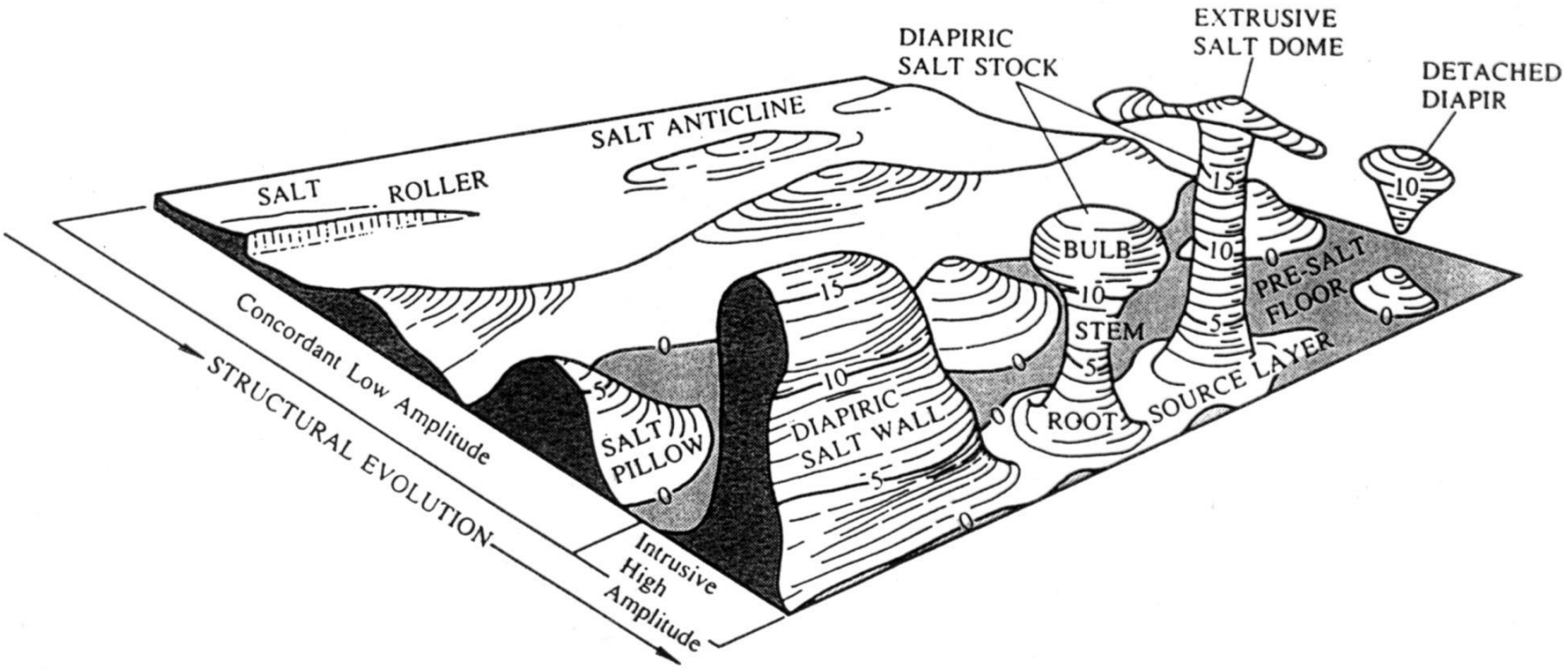

Figure 10-11
The main configurations of salt structures. Structure contours are in arbitrary units. Larger features such as salt nappes cannot be shown at this scale. [Jackson and Talbot, 1986, p. 306.]

čtení:

M.E.Tucker: Sedimentary petrology. 3rd ed. Blackwell, 2001.
H. Blatt (1992): Sedimentary Petrology. Freeman &Co., New York.
G.S.Odin a A.Matter (1981): De glauconiarum origine. Sedimenntology, 28, 611-641.
C.R.Glenn and 15 others (1994): Phosphorus and phosphorites: Sedimentology and environments of formation. Eclogae Geol. Helv., 87, 3, 747-788.
S.D.Killops a V.J.Killops (1993): Organic Geochemistry. Longman, New York.
G.H.Taylor et al. (1998): Organic Petrology.Berlin.
B.P.Tissot a D.H.Welte (1978): Petroleum Formation and Occurrence. Springer, Berlin.